Version of Record: https://www.sciencedirect.com/science/article/pii/S175058362100253X
Manuscript_609f316d45df543233d1aa6753ba3f7a

# Joint impedance and facies inversion of time-lapse seismic data for improving monitoring of $CO_2$ incidentally stored from $CO_2$ EOR

César Barajas-Olalde [a*], Alan Mur [b], Donald C. Adams [a], Lu Jin [a], Jun He [a], John A. Hamling [a], Charles D. Gorecki [a]

[a] *Energy & Environmental Research Center, 15 North 23rd Street, Stop 9018, Grand Forks, ND 58202-9018, USA*

[b] *Ikon Science Americas, 12140 Wickchester Lane, Suite 400, Houston, TX 77079, USA*

* *Corresponding Author: E-Mail: cbarajas@undeerc.org*

*Phone: 1-701-777-5414; Fax: 1-701-777-5181*

*E-Mail: amur@ikonscience.com*

*E-Mail: dadams@undeerc.org*

*E-Mail: ljin@undeerc.org*

*E-Mail: jhe@undeerc.org*

*E-Mail: jhamling@undeerc.org*

*E-Mail: cgorecki@undeerc.org*

*Recommended for inclusion in the GHGT-15 Special Issue*



© 2021 published by Elsevier. This manuscript is made available under the Elsevier user license
https://www.elsevier.com/open-access/userlicense/1.0/

## ABSTRACT

Time-lapse seismic monitoring is an effective and proven technology for mapping the distribution of $CO_2$ in a subsurface reservoir. When injected $CO_2$ displaces other reservoir fluids, porous-medium properties are changed and thus the seismic impedance changes, causing time-lapse seismic amplitude differences in the injection zones. The analysis and interpretation of images created from these amplitude differences can provide information about reservoir architecture and the $CO_2$ migration within the reservoir. Incorporating seismic inversion and rock physics into the interpretation of time-lapse seismic data can considerably improve the modeling and monitoring to detect and assess the location of $CO_2$ over time. The joint inversion method presented in this paper has an integral representation of the geology in the inversion algorithm using elastic facies, which provides information about the spatial distribution of the geologic heterogeneities controlling the movement of fluids in the reservoir. The method was successfully applied to time-lapse seismic data from a mature oil field undergoing $CO_2$ enhanced oil recovery. The estimated seismic acoustic impedances and facies reflect the characteristics of individual geologic facies and fluid conditions of the reservoir subject to $CO_2$ injection. The probabilities estimated by the joint impedance and facies inversion for the reservoir's litho-fluid facies can be used for forecasting $CO_2$ saturation and pressure changes within the target reservoir.



**KEYWORDS**: seismic inversion, time-lapse seismic, 4D seismic, $CO_2$ storage, enhanced oil recovery, seismic monitoring, facies, rock physics, reservoir simulation.

## 1. INTRODUCTION

The success of geophysical methods in carbon capture and storage projects has been illustrated in the literature (e.g., Davis et al., 2003; Arts et al., 2004; Alnes et al., 2008; White, 2009, 2011; Chadwick et al., 2010; O'Brien et al., 2010; Bhuyian et al., 2012; Dodds et al., 2013; Park et al., 2013, Carrigan et al., 2013; Tucker et al., 2016; Schmidt-Hattenberger et al., 2016; Burnison et al., 2017; Dupuy et al., 2017; Furre et al., 2017; Zhao et al., 2017; Roach et al., 2017; Salako et al., 2017, 2018; Wan et al., 2018; Macquet et al., 2019; Barajas-Olalde et al., 2020; Trautz et al., 2020; White et al., 2021; Pevzner et al., 2021). The seismic method is the most popular geophysical method mainly because of its high horizontal resolution. When the seismic method is applied to monitoring time-lapse changes of a reservoir subject to $CO_2$ injection, at least two data sets are acquired. The baseline data set is acquired before the $CO_2$ injection, and the monitor data sets are acquired after the $CO_2$ injection has been initiated. Maps of seismic amplitude differences from baseline and monitor surveys can be used to interpret the time-lapse changes in the reservoir due to $CO_2$ injection. Incorporating seismic inversion and rock physics into the interpretation can considerably improve the modeling and monitoring to detect stored $CO_2$ and assess the location of the $CO_2$ distribution in the reservoir over time.

Seismic inversion transforms seismic reflection data into reservoir elastic properties (i.e., P-wave velocity (Vp), S-wave velocity (Vs), density (Rho), acoustic impedance (AI), shear impedance (SI)] that produced the reflections) (e.g., Sen and Stoffa, 2013). When seismic inversion is integrated with rock physics, elastic properties can be quantitatively transformed into geologic properties (e.g., porosity, lithology, fluids) for reservoir characterization (e.g., Mavko et al., 2009).

66 The main challenges in seismic inversion are the different sources of uncertainties such as
67 observation errors, limited bandwidth of the seismic data, seismic, well logs, data processing, and
68 rock physics modeling errors (Bosch et al., 2010; de Figueiredo, 2018). Therefore, a Bayesian
69 framework is a natural option for a seismic inversion (Bosch et al., 2010, and literature therein; de
70 Figueiredo, 2018, and literature therein).

71 The solution of the Bayesian inverse problem is defined by a posterior distribution
72 (Tarantola, 2005), which is conditioned to all the available observation data, the errors, and prior
73 knowledge of the subsurface, such as spatial correlations, depositional trends, and background
74 model (de Figueiredo, 2018).

75 In the last decades, extensive activities have been conducted to develop Bayesian algorithms
76 that incorporate uncertainty quantification, geology, rock physics, and geostatistics in seismic
77 inversion (e.g., Buland and Omre, 2003; Gunning and Ginsky, 2007; Bosch et al., 2010; Ulvmoen
78 and Omre, 2010; Kolbjørnsen et al., 2016; Fjeldstad and Grana, 2018; Kemper and Gunning, 2014;
79 Grana et al., 2017; de Figueiredo et al., 2018; Grana, 2018; Gunning and Sams, 2018; Waters et
80 al., 2019; Gunning and Huntbatch, 2020).

81 Instead of a two-step inversion in which elastic parameters are estimated first and then the
82 elastic parameters are mapped to reservoir properties, one-step inversion (i.e., joint inversion) to
83 reservoir properties is preferred (Connolly, 2017). Joint inversion algorithms allow the integration
84 of a wide range of geological information and can predict facies directly from seismic reflection
85 data (e.g., Rimstadt et al., 2012; Kemper and Gunning, 2014; Grana, 2018; Gunning and Sams,
86 2018; Waters et al., 2019; Azevedo et al., 2020).

87 We apply a joint impedance and facies inversion (Ji-Fi) technology (Kemper and Gunning,
88 2014) to two seismic data sets to monitor the time-lapse changes within the reservoir as a result of

$CO_2$ EOR (enhanced oil recovery) operations at a mature oil field. Ji-Fi estimates a three-dimensional (3D) facies classification scheme based on Bayesian principles, geological facies as priors, and powerful image-processing techniques. The oil field is in southeastern Montana near the northeastern edge of the Powder River Basin in the United States.

## 2. GEOLOGICAL SETTING AND $CO_2$ EOR

The oil field is a complex stratigraphic trap located structurally on a shallow monocline with a 1°–2° dip to the northwest and an axis trending southwest to northeast for approximately 32 km (Bosshart et al., 2015; Sharaf and Sheikha, 2021). The 6–9-m thick oil-bearing reservoir is part of the Lower Cretaceous Muddy Formation at a depth of approximately 1372 m (Fig. 1). This formation is dominated by high-porosity (15%–35%), high-permeability (150–1175-mD) sandstones (Saini et al., 2012). The Muddy Formation has been divided into three informal members based on Molnar and Porter's study (1990), consisting of (from bottom to top) the Rozet Member, the Bell Creek Sand Interval, and Springen Ranch, (see Fig. 1). The Rozet Member overlies the Skull Creek Shale and consists of a 0.15–0.9-m sand marking the Skull Creek–Rozet contact and an overlying 1.5–3.0 m of shale/siltstone. The Bell Creek Sand Interval overlying the Rozet Member is described as having up to three different sand lobes (vertically). The Springen Ranch Member overlies the Bell Creek Sand Interval and is generally silty with some sand content. Overlying the Springen Ranch Member is the Shell Creek Shale. The overlying Lower Cretaceous Mowry Formation provides the primary seal, preventing migration to overlying aquifers and to the surface (Bosshart et al., 2015). The $CO_2$ injection target reservoir is a heterogeneous sand with fluvial channels, barrier bars, lagoonal, and nearshore facies leading to compartmentalized geobodies separated by permeability barriers and baffles, which lead to complex fluid

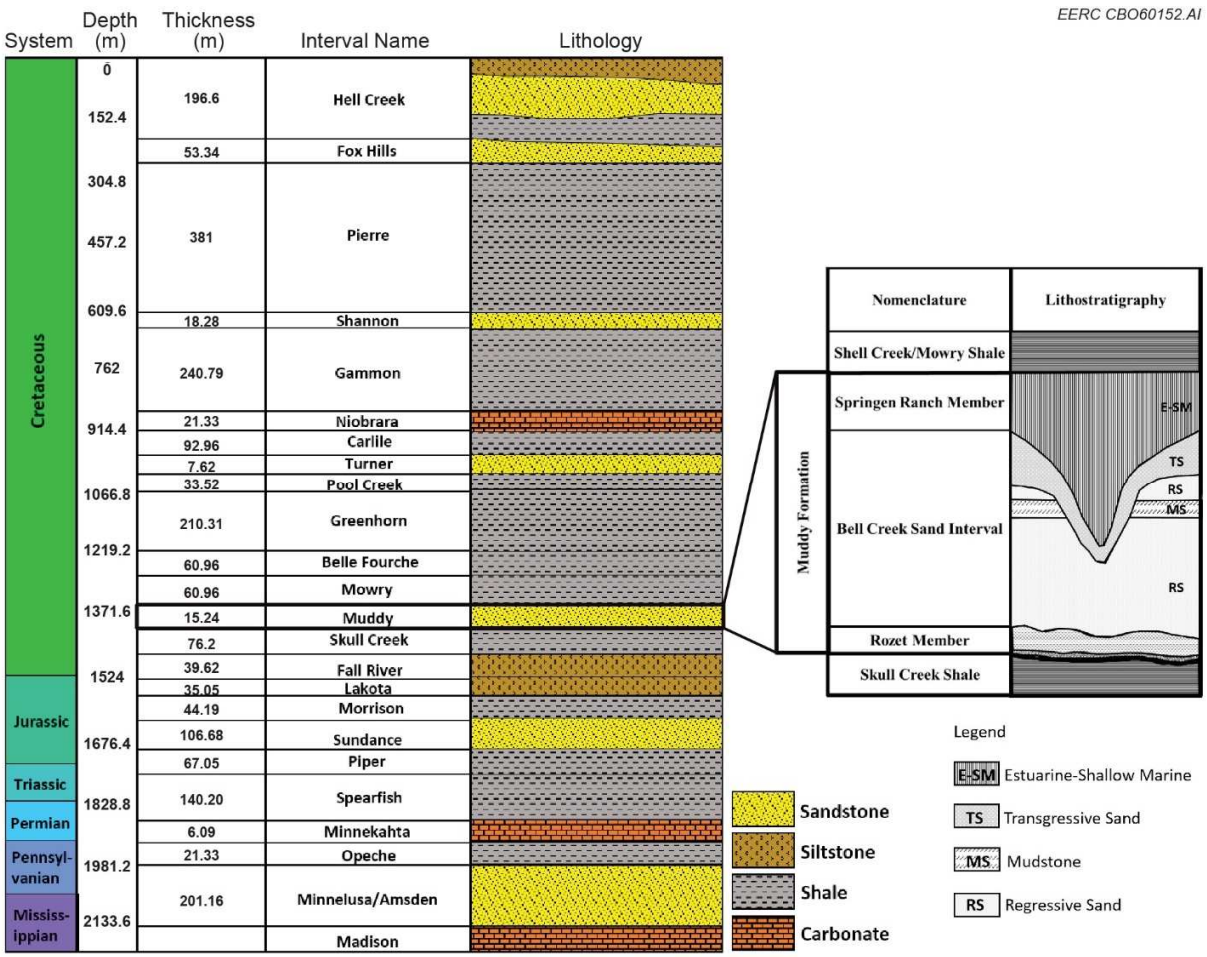


**Figure 1.** Stratigraphic column of the study area and simplified reservoir stratigraphy (modified after Burnison et al., 2017).

communication pathways between various compartmentalized geobodies (Bosshart et al., 2015). The permeability barriers have been inferred from a) well penetration with little or no reservoir-quality sandstone; b) wells with high water cut only a short distance updip from wells with notable oil and/or gas production; c) significant variability in pressure, volume, temperature (PVT) properties of produced hydrocarbons; d) considerable reservoir pressure differences, sometimes over very short distances within the field; and e) 4D seismic difference maps and seismic attributes (Spakiewicz et al., 1988; Honarpour et al., 1989; Molnar and Porter, 1990; Bosshart et al.; 2015, Burnison et al., 2017; Salako et al., 2017).

Since the discovery of oil and gas in the 1960s, the oil field has undergone primary and secondary recovery that resulted in a gradual production decline leading to tertiary oil recovery implementation using $CO_2$ flooding (Hamling et al., 2013). $CO_2$ EOR is progressing through nine schematical development phases (regions within the oil field). Up to 1.6 million cubic meters of $CO_2$ per day is supplied by natural gas-processing plants located approximately 373 km from the study area (Burnison et al., 2017). This study focuses on Development Phases 1 and 2. Each phase was pressurized by water injection in preparation for $CO_2$ EOR. $CO_2$ injection began in Phase 1 in May 2013 and Phase 2 in December 2013.

Extensive work has been conducted at the Energy & Environmental Research Center (EERC) to build a geologic model incorporating 3D seismic data, well logs, and core data (Jin et al., 2016). The model includes depositional facies that can constrain petrophysical property distributions, enabling a better history match and more accurate predictive simulations of pressure response, injected/produced volumes, and saturation changes. Fig. 2 shows the facies interpreted in Development Phases 1 and 2 and an adjacent development phase within the Bell Creek Sand Interval Member.

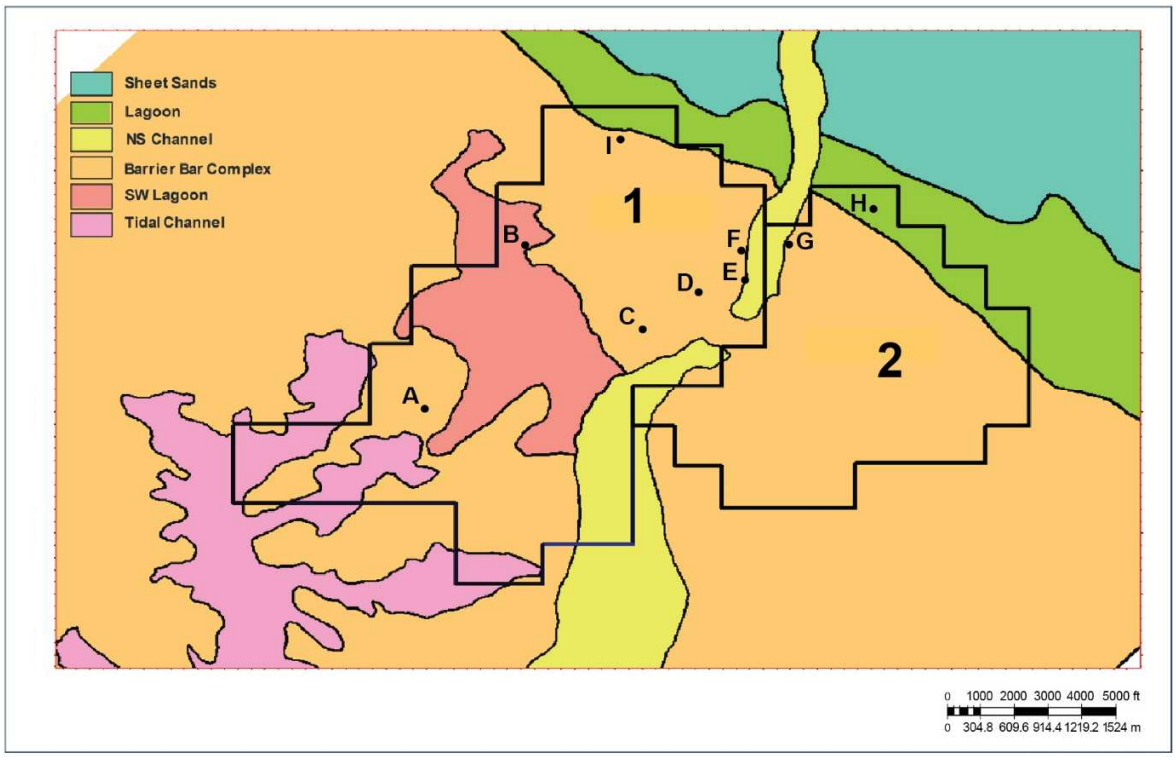


**Figure 2**. Geological facies interpreted in the study area: lagoon, barrier bar complex, North-South channel, and tidal channel. The polygons represent the study area (Development Phases 1 and 2). The boundaries of the map represent the area of the seismic surveys. The wells used in this study are represented by the letters A through I.

## 3. JOINT IMPEDANCE AND FACIES INVERSION

Rock physics and seismic inversion are fundamental tools of quantitative reservoir characterization. In this process, the impedance and elastic parameters estimated by the inversion of seismic data can be related to rock properties using rock physics models. Ji-Fi seamlessly integrates rock physics and inversion using seismic facies (Kemper and Gunning, 2014).

Ji-Fi is model-based seismic inversion defined as a Bayesian approach, and it is expressed as follows (Waters et al., 2019; Gunning and Huntbatch, 2020):

$$P(m, F \mid y) \sim L(y \mid m) * P(m \mid F) * P(F) \quad (1)$$

where $m$ is the elastic model (Vp, Vs, Rho); $F$ is the facies variable at discrete locations in the inversion volume; $y$ is seismic data; $L\,(y \mid m)$ is the likelihood of the synthetic seismic generated by the forward model; $P\,(m \mid F)$ is the probability density function of the rock properties given the facies prior model; and $P\,(F)$ is the facies distribution aligned to the stratigraphy.

As inferred from Equation 1, Ji-Fi solves for the distribution of elastic properties and facies. The low-frequency model (LFM) of elastic parameters required in seismic data inversion to account for the band limit and the lack of low-frequency signal in the seismic data is a product of the inversion.

Contrary to standard inversion algorithms that build LFMs by interpolating well logs within a structural and stratigraphic framework, Ji-Fi uses a rock physics models defined by facies to build an LFM model per facies. The rock physics model for each of the facies is defined by a depth trend in terms of the elastic parameters Vp, Vs, Rho, AI, SI, and their relationships. Each component of the model has associated uncertainties. The rock physics models are assumed to apply over an entire study area and can be extrapolated to depths greater than the well control.

The inputs for the basic Ji-Fi workflow are the following: a set of estimated prior facies proportions within defined stratigraphic intervals, LFM models (depth-dependent rock physics models) for each expected facies and uncertainties for each facies, a set of seismic partial angle stacks, estimated noise in the partial-angle stacks, and seismic wavelets with estimated individual root mean square (RMS) error, which are used to solve for both the most likely facies model and its corresponding set of impedances (Waters et al., 2016). A detailed analysis of the requirements of the prior input information and its uncertainty for the Ji-Fi workflow is given by Waters and Kemper (2018) and Gunning and Sams (2018).

178 The selection of the (reservoir and nonreservoir) facies to invert for is based on the study
179 area's lithologies and fluids, their relevance to a geologic interpretation, and their separation in the
180 elastic domain. According to Equation 1, seismic data are used to constrain the distribution of the
181 facies in the Ji-Fi scheme. Therefore, the facies must have some degree of separation in the elastic
182 domain. Furthermore, a compromise must often be made on selecting the number of facies based
183 on the degree of overlap in the elastic domain. Since these requirements might not be compatible
184 with the idealized geologic facies definition, the facies should be called elastic facies (Sams et al.,
185 2016).

186 The LFM models for each expected facies can be estimated from a depth trend analysis
187 (DTA) of P-wave velocity (Vp), shear-wave velocity (Vs), density, and impedances derived from
188 well logs, one-dimensional (1D) basin models, or analog fields. The LFM trends are referenced to
189 a single datum, which reduces the need for detailed seismic interpretation. The crossplotted depth
190 trends (Vp vs. density, Vp vs. Vs, AI vs. SI, AI vs. Vp/Vs), and an assessment of their uncertainty
191 are used for quality control. An essential feature of the Ji-Fi approach is that the LFM trends are
192 not interpolated between wells. Therefore, the depth trends are not compromised by bias in
193 interpreting seismic horizons or interpolation artifacts. Since the facies represented in the depth
194 trends depend on rock physics models, more plausible elastic properties estimates can be obtained.

195 Fig. 3 depicts a diagram of a simplified Ji-Fi scheme with only the AI component and sand
196 and shale facies. The Ji-Fi algorithm iteratively inverts seismic (trace by trace) for impedances
197 given facies and then inverts for facies given an impedance model until convergence is reached.
198 The convergence criterion is founded on matching synthetic seismic models with real seismic trace
199 data until the misfit between the two is reduced to an acceptable level. It should be noted that
200

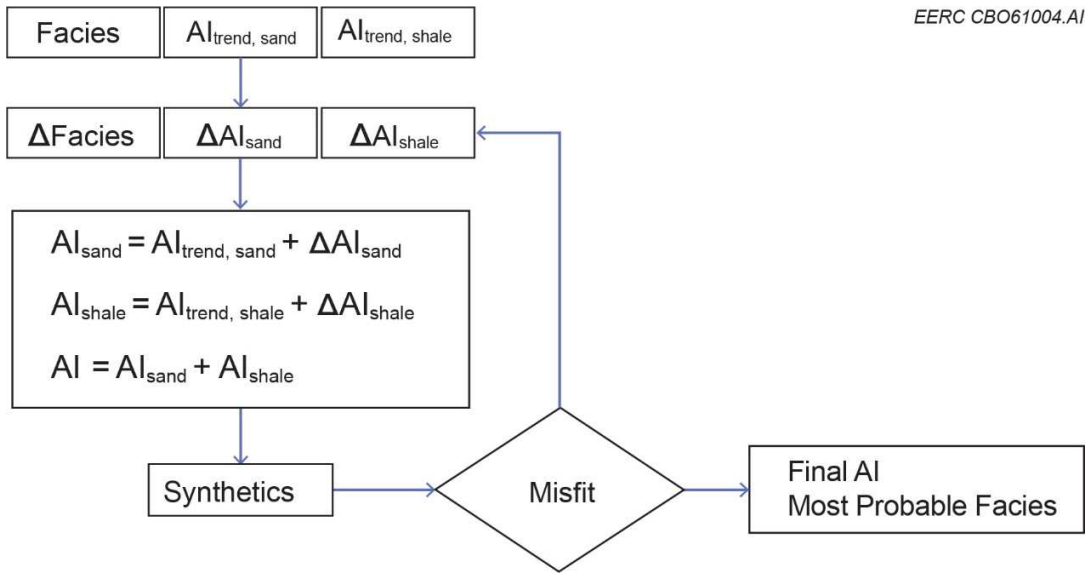


**Figure 3.** Simplified diagram of the Ji-Fi scheme for an acoustic inversion (modified after Waters et al., 2016).

the facies result depends on the last set of impedance results and vice versa. This scheme implies that better impedances lead to better facies estimates and vice versa at each workflow iteration. The inversion can be constrained to promote facies continuity (lateral or vertical) and to honor realistic geologic and hydrodynamic facies conditions (Kemper et al., 2017). The Ji-Fi workflow outputs are Vp, Vs, density, and the most probable facies, with standard deviations and probabilities. Kemper and Gunning (2014) and Gunning and Huntbatch (2020) report details of the Ji-Fi algorithm.

## 3.1 Input data

### *3.1.1 Seismic data and horizons*

The Ji-Fi approach requires seismic data for inversion and seismic horizons to constrain the time and depth model relationships. The 3D seismic data sets to monitor the time-lapse changes within the reservoir due to the $CO_2$ EOR operations correspond to the September 2012 baseline survey acquired prior to $CO_2$ injection activities and the October 2014 monitor survey acquired

after the start of commercial $CO_2$ EOR operations. The 2014 monitor survey overlaps the 2012 baseline survey at Development Phase 1 and part of Development Phase 2. At the time of acquisition of the monitor survey, the Phase 1 and 2 areas had undergone $CO_2$ injection for 18 and 10 months, respectively. A summary of repeat 3D seismic data acquisition and the data processing workflow is included in Appendix A of Salako et al. (2018). The seismic reflection of the 6–9-m-thick Bell Creek sand reservoir is that of a thin-bed response, composed of entering and exiting reflections from the Springen Ranch and Skull Creek intervals, respectively, near the 11-ms resolution limit of the embedded wavelet derived from an amplitude spectrum with a bandwidth of approximately 10–48 Hz estimated from a 500-ms window centered in the zone of interest (Burnison et al., 2014, 2017). Sets of baseline (2012) and monitor (2012) angle stacks (reverse polarity, common midpoint, and angle gathers stacked over $10^o$ angle ranges to 5°, 15°, 25°, 35° midpoints) were used as input for our study. A seismic cube obtained from the stacking of the prestack time-migrated (PSTM) offset gathers was used to interpret time and depth horizons. The interpreted horizons used to build the model for the seismic inversion are the following: Horizon 1: a strong event above the reservoir (this horizon was used as a datum for the DTA); Springen Ranch: top of the reservoir; Skull Creek—bottom of the reservoir and low boundary of Bell Creek (LBBC)—a strong event below the reservoir. Fig. 4 shows a time-lapse amplitude RMS difference map, calculated between the Springen Ranch and Skull Creek. The difference is computed as the monitor (2014) minus baseline (2012) survey. The high sensitivity of the seismic

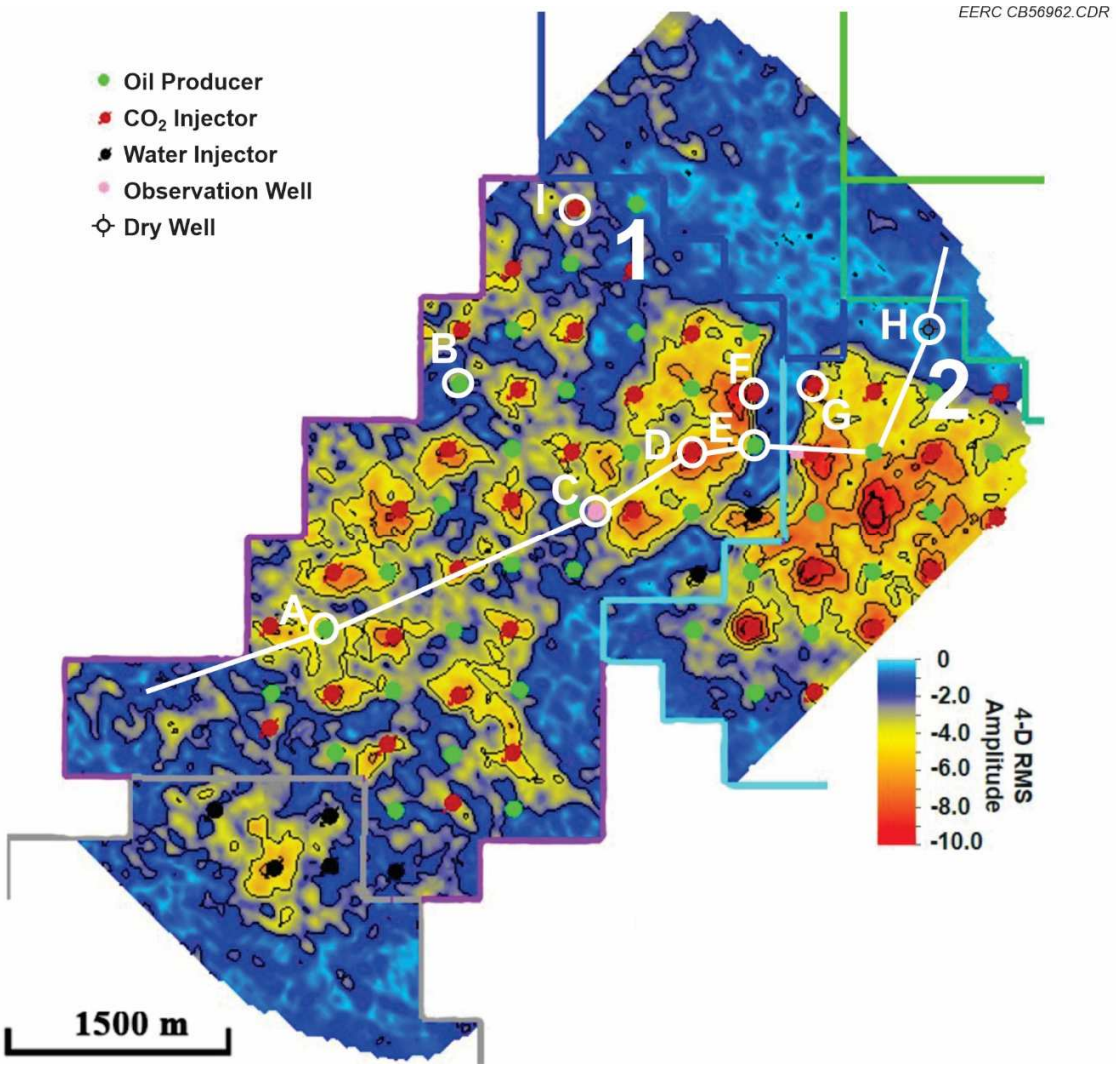


**Figure 4.** Time-lapse amplitude difference map of monitor (2014) minus baseline (2012) calculated as a summation of RMS amplitudes at the reservoir interval between the Springen Ranch and the Skull Creek horizons. The wells in Development Phases 1 and 2 are shown with the following symbols" Green dot – oil producer, red dot – $CO_2$ injection well, black dot – water injector, pink dot – observation well, black circle with lines – dry well, white circle – wells used in this study, white line – cross section along some of the wells used in this study (modified after Salako et al., 2017).

signal to the changing fluid properties within the reservoir induced by $CO_2$ injection is clearly observed in the 4D seismic amplitude response (warm colors). The interpretation of the map (Burnison et al., 2017; Salako et al., 2017) indicates the permeability barriers in Phases 1 and 2 associated with the little time-lapse response to low-permeability deposits resisting fluid flow and

pressure dissipation. Burnison et al. (2017) and Salako et al. (2017) interpreted the apparent high seismic amplitude response to the $CO_2$ injection in Phase 2 with a shorter period of $CO_2$ injection (10 months) than in Phase 1 (18 months) to greater change in sustained pore pressure that occurred in Phase 2 before $CO_2$ injection.

### *3.1.2 Well data*

After data conditioning, eight wells with complete log suites for rock physics modeling and quantitative well tie were used in the Ji-Fi workflow. The location (and type) of these A (producer), B (producer), C (observation), D ($CO_2$ injector), E (producer), F ($CO_2$ injector), G ($CO_2$ injector), and H (dry hole) wells in the study area is shown in Figs. 1 and 4 Three of these wells (A, C, and G) were extensively geologically sampled with sidewall and whole core.

### *3.1.3 Geologic data*

Geologic analysis of the well data included a description of whole cores. Sidewall cores lab work was done, including x-ray diffractometry (XRD), scanning electron microscopy (SEM), porosity and permeability measurements, and petrology. The analysis of thin sections and SEM mineral maps reported by Eylands et al. (2013) indicates that most of the sidewall cores from the C well are grain-supported and that the grain cement is dominantly clay. A small volume of quartz cement is also present. Braunberger et al. (2013) studied core from the Bell Creek reservoir and reported that carbonate may also be a locally important cement. The significant differences in the porosity and permeability of the Muddy Formation sand intervals of the Bell Creek reservoir can be attributed to clay concentration and distribution within the samples (acting as a contact cement). Decreased porosity and permeability can be attributed to higher clay concentrations, especially kaolinite, filling the pore spaces between sample grains (Eylands et al., 2013).

## 3.2 Data conditioning

### *3.2.1 Seismic data*

PSTM offset gathers were converted to the partial-angle stacks required for the Ji-Fi prestack approach. Four partial-angle stacks were created: near (0–10 degrees), mid (10–20 degrees), far (20–30 degrees), and ultrafar (30–40). Although the original time-lapse conditioning scheme was satisfactory, additional data conditioning was performed. First, a 2–4–65–80-Hz finite impulse bandpass filter was applied to each partial-angle stack to remove high-frequency noise. After that, a robust time-shift estimation between near, mid, and far angles of the baseline and monitor data sets was applied to remove normal moveout correction (NMO correction) residual time-shifts included in the data processing. The time-shift estimation parameters were a 175-ms correlation window with a time-shift averaging over a three-trace radius followed by a 90-ms time-shift smoothing window. Fig. 5 depicts the results of the data conditioning on baseline (top) and monitor (bottom) stacked cross sections shown as a white line in Fig. 4. The A, C, D, and E wells and horizon 1, Springen Ranch, Skull Creek, and LBBC horizons are also depicted in the figure as reference.

### *3.2.2 Well log data*

To assess any issues in the data acquisition and processing of the logs that can affect the inversion results, quality control of the available well logs was conducted. Any spikes and noise bursts were replaced, and gaps were filled using either spline functions away from the zone of interest or more robust rock-physics-based methods within the zone of interest. Histograms were used to assess the log distribution between the three wells A, C, and G with the complete sets of elastic logs (P-wave sonic, S-wave sonic, and density) in the Bell Creek interval from field data

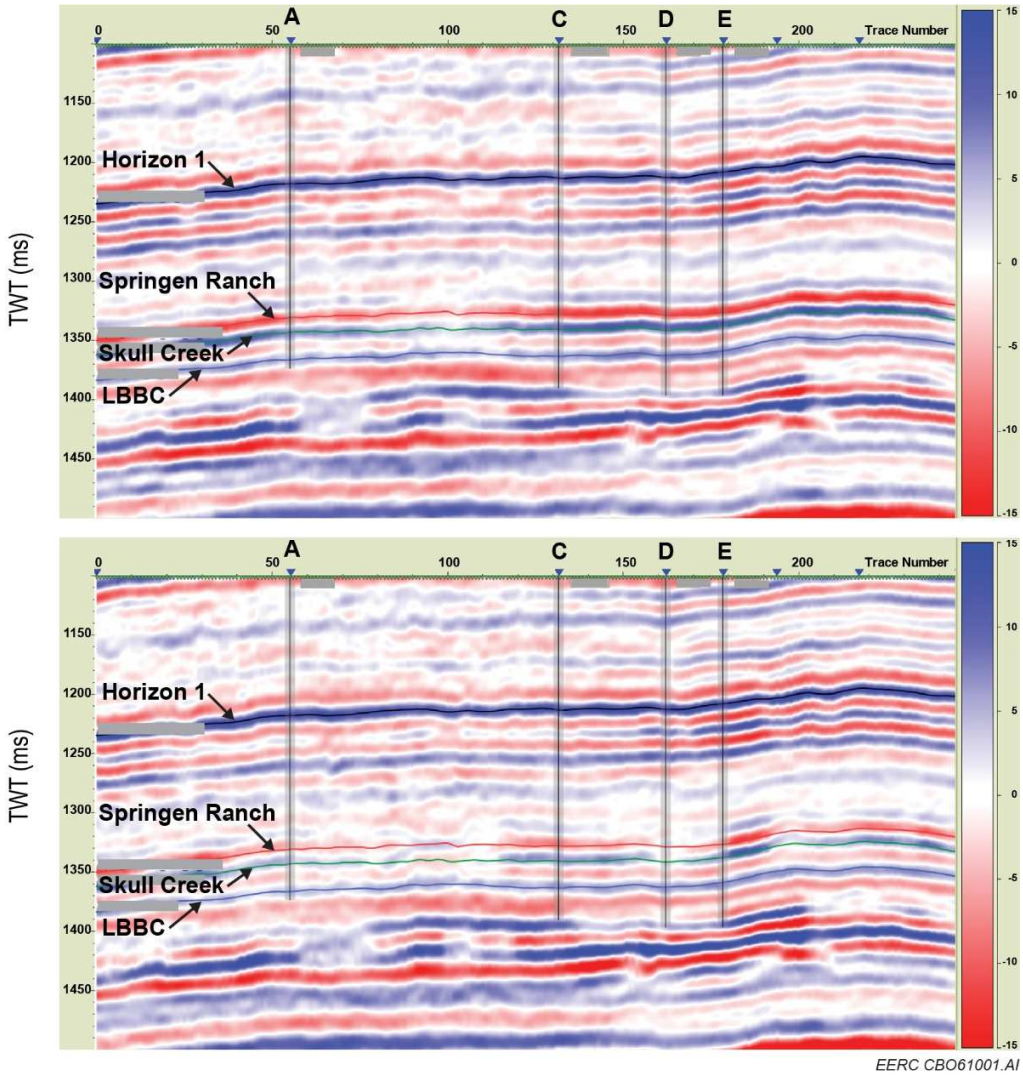


**Figure 5**. Cross section of baseline (top) and monitor (bottom) stacks after data conditioning. The cross section intersects the A (producer), C (observation), D ($CO_2$ injector), and E (producer) wells. Horizon 1, Springen Ranch and Skull Creek, and the LBBC horizons are shown as a reference. The cross sections do not include the part of the line where the H (dry) well is located.

acquisition. Consistent results were obtained between wells, except for the density in the A well, which had a wider distribution than expected. However, the values are still in the range for sandstone reservoirs based on Appendix A1 of Mavko et al. (2009).

Since the other available wells do not include fundamental logs with elastic properties for the application of Ji-Fi, a combination of rock physics methods with empirical relationships were

used to estimate Vs for B, D, E, F wells, and density for D, E, F wells. A hybrid method was used to estimate Vs for the defined working intervals: a modified Gassmann approach (Mavko et al., 2009) for the interval representing the reservoir. This approach is based on the linear form of Gassmann's equation to estimate Vs when the rock is hydrocarbon-saturated. The linear form of Gassmann's equation expresses the change in bulk modulus due to fluid substitution as a function of the intercept porosity parameter (PoR) (Mavko and Mukerji, 1995). As the fluid modulus is typically much less than the mineral modulus and the Gassmann's equation predicts no change in shear modulus during fluid substitution, the linear form of Gassmann's equation can be expressed as a function of the P-wave modulus and used to estimate the sonic velocity (Vp) for a brine-saturated sample from the measured log data in a hydrocarbon interval. The Greenberg–Castagna approach (1992) can then be used to calculate the associated saturated Vs. The final step is to use the conventional Gassmann's equation to perform a fluid substitution of the brine-saturated properties to reestimate the Vp, Vs, and density of the in situ saturation. The generated Vs product is the output of the process. Input data for this approach are porosities, in situ fluids, and Vp to predict water-saturated Vp–Vs–density and then substituted for in situ fluids. Empirically calibrated Vp–Vs relationships were used to predict the overburden (from Horizon 1 to Shell Creek markers) and the underburden (from Rozet to Skull Creek markers) working intervals. These relationships are given by the linear relationship: Vs = Vp*x + c. The constant values x and c can be derived from a linear fit using crossplots. In the case of density prediction, while linear Vp–density relationships calibrated [1) (Rho = Vp + constant) / constant; 2) Rho = Vp * constant + constant; the constants are derived from crossplots] per working interval were used for working intervals other than the Bell Creek interval, a mix of two methods scaled by porosity was used for the Bell Creek interval. The first method uses mineral volumes, calibrated mineral densities,

porosity, fluid logs, and fluid densities to predict log densities. In the second method, shale density is locally calibrated between the Springen Ranch and Skull Creek markers for fluid substitution (density of shale = 2.338) from a fluid subshale average set previously calculated. Attempts were made to predict Vp for some wells. However, it was impossible to define a method to predict all the working intervals for all the wells correctly. After data conditioning, the A, B, C, D, E, F, G, and H wells were considered in the Ji-Fi workflow.

### 3.3 Well tie and wavelet extraction

Well to seismic data (full stacks and partial stacks) ties were performed to estimate the wavelets for the inversion. The A, B, C, G, and H wells were selected for this process as the original and predicted logs were adequate in the depths from Horizon 1 to the LBBC horizons, which were considered as the inversion model limits. Since D and E wells did not fulfill this requirement, they were used for calibration purposes. The effective wavelet length was between 80–128 ms, and the analysis window was approximately 400 ms. An initial bulk shift was made to maximize correlation over the analysis window with a statistical 180-degree phase rotation wavelet or with a group average Bayesian wavelet (simultaneous multiwell wavelet estimation method). Next, the Roy White method (White, 1997) was used on the selected wells and surrounding seismic data. After estimating the deterministic wavelets at each well, an average wavelet was created and used to make a final bulk shift at all the well locations.

Comparable results to the well-to-full stack seismic data ties were obtained with partial stacks following the same methodology for full stacks mentioned above. However, in this case, one wavelet is estimated for each partial stack. While an averaged (Roy White) wavelet was estimated for the near angles, averaged Bayesian wavelets were estimated for the mid and far

angles. An example of the synthetic-to-seismic tie for the C well using baseline seismic data is shown in Fig. 6. An excellent-quality tie was observed for the eight wells used in this study.

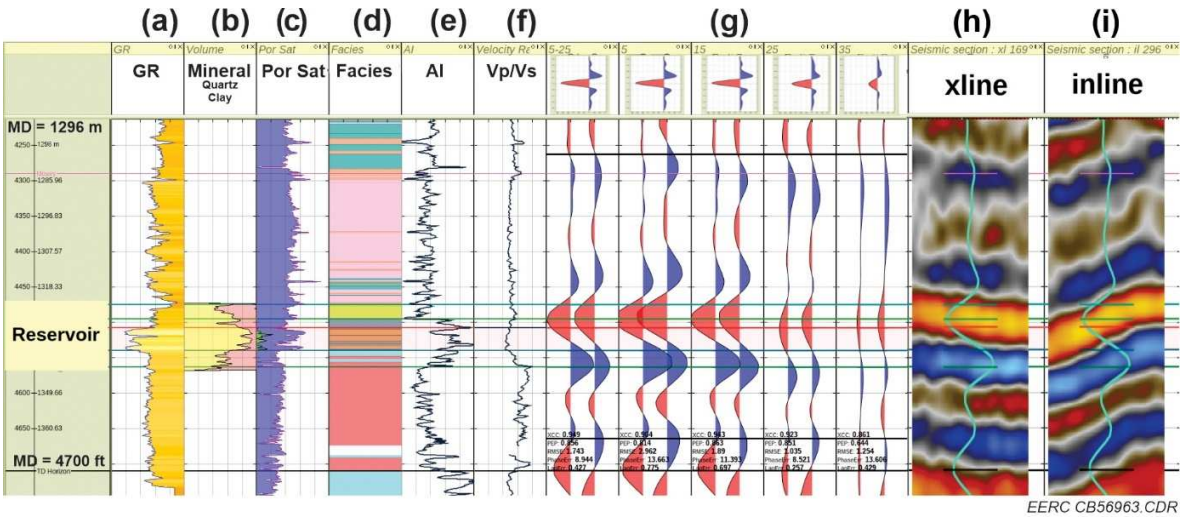


**Figure 6**. Well-tie and AVO QC at the C well: a) gamma ray with light fill identifying sands; b) volume fraction set of quartz (yellow) and clay (pink); c) porosity with fluid saturation (trace oil); d) petroelastic facies classification; e) AI; f) Vp/Vs ratio; g) synthetic-to-seismic ties (full stack, 5°, 15°, 25°, and 35° angle stacks). The range of angle stacks is ±5° from indicated angle with wavelets in the header (equal amplitude ranges for wavelets); h) crossline; and i) in-line section QC with synthetic overlay. It should be noted that the reverse-polarity wavelet convention (an increase in impedance results in a negative reflection) was used in this study.

## 4. ROCK PHYSICS

Rock physics analysis can estimate changes in the reservoir elastic properties due to changes in stress, pore pressure, fluid type, saturation, and mineralogy variations.

### 4.1 Rock properties

As the A, C, and G wells originally had shear sonic logs, they were used for rock physics analysis. Sidewall cores in the A, C, and G wells were used to link wireline measurements with the study area's geology. A close agreement of bulk density, porosity, and lithology volumes with corresponding values from wireline logs was expected after allowing for differences due to depth

uncertainty, resolution, and sampling bias. In general, a ±0.61-m depth uncertainty for sidewall cores in the three wells was observed. The following comparisons were conducted, as shown in Fig. 7:

- Bulk densities derived from core grain density and core porosity. The results were compared with density log, good agreement between both types of density measurement was observed.
- Measured core porosities vs. various porosity logs (Schlumberger RST Advisor, neutron, sonic, density). The best agreement was found with density porosity (DPHI) on a sandstone matrix. This finding is consistent with the results reported by Sutherland (2011) and Pasternack (2009). A density of 2.65 g/cm3 was used to calculate the sandstone density porosity curve. This value is close to 2.60–2.63 g/cm3 for the Bell Creek clay grain density reported by Pasternack (2009).
- Mineral types and volumes estimated from XRD analysis of sidewall core samples vs. results from Schlumberger's RST SpectroLith estimates WCAR (carbonate), WQFM (quartz, feldspar, mica), and WCLA (clay) derived from wireline logs. The log data are consistent with the XRD data. The comparison suggests that the WCLA log provides a reasonable estimate of the weight fraction of clay. It can also be inferred from the XRD results that kaolinite is the dominant clay in the Bell Creek interval. The three high-quality logs used to compare with sidewall cores were considered the initial reference for rock physics analysis and inversion tests.

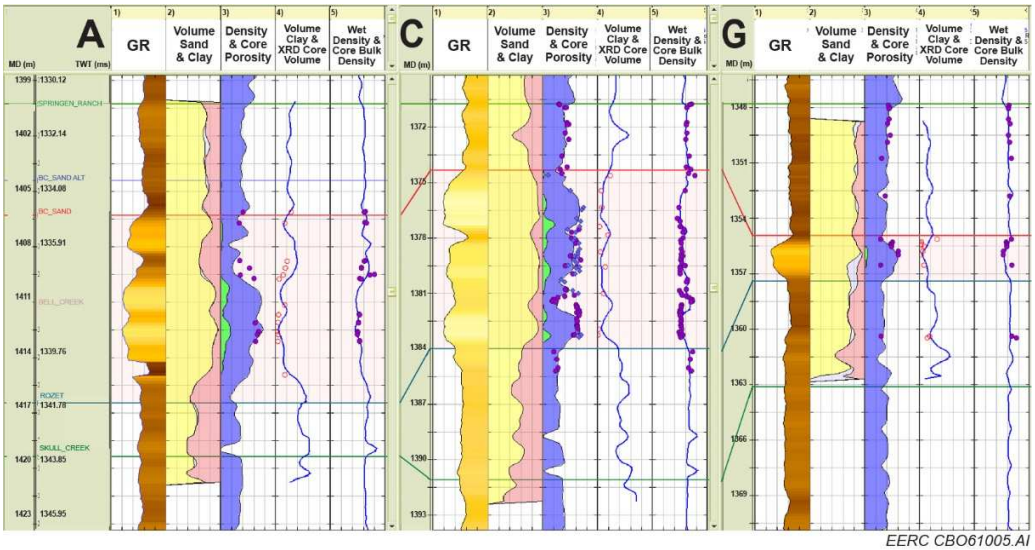


**Figure 7.** Comparison of core measurements of porosity, volume clay, volume carbonate, and bulk density with log data from the A, C, and G wells. The tracks from left to right in each well are gamma ray (GR), volume (yellow sand, pink clay), density porosity (DPHI) with core porosity, volume clay (orange), or carbonate (blue) with core volume from XRD, wet density with core bulk density. Core bulk density was calculated from grain density and porosity, assuming the fluid density of 1.0 g/cm$^3$.

## 4.2 Muddy Formation

The Muddy Formation comprises three members: Springen Ranch, Bell Creek, and Rozet. All three members are seismically thin and well below tuning. In combination, they reach a sufficient thickness that seismic reflections are associated with the approximate top and base of the Muddy Formation. Hence, all the members' elastic properties contribute to the apparent impedance contrasts sensed by the reflections. After fluid substitution to replace any oil saturation with brine, Fig. 8 shows that the elastic properties of all three units overlap to some extent. The Bell Creek at any porosity has, in general, a faster Vp and Vs than Rozet. The Rozet has a smaller range of porosities and is generally slower than the Bell Creek. Springen Ranch properties are near the transition between Bell Creek and Rozet and are entirely contained within the data cloud formed by the Bell Creek and Rozet.

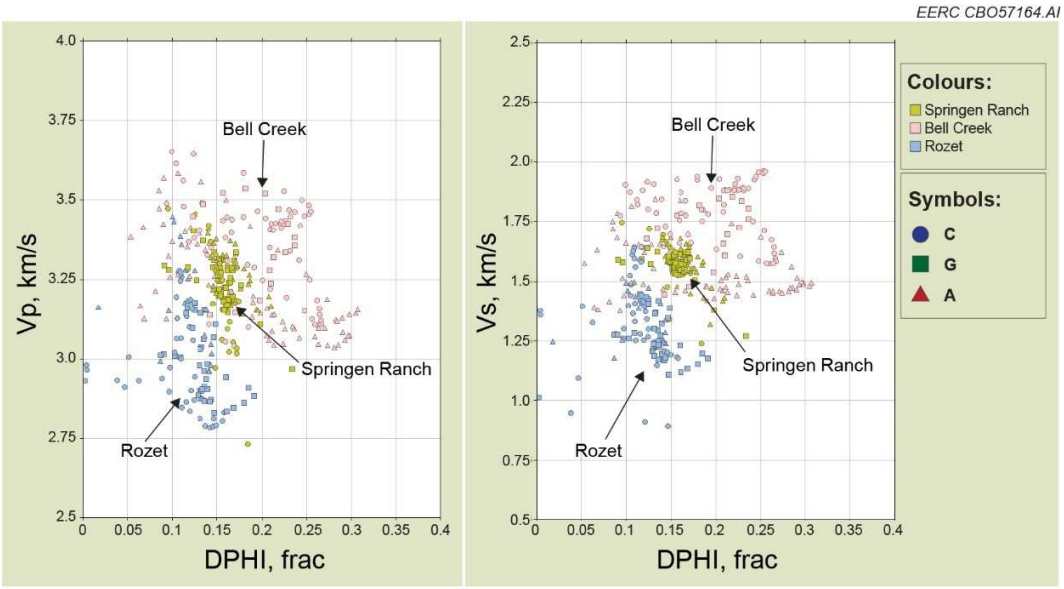


**Figure 8**. Muddy Formation. Springen Ranch (yellow) plots within the Bell Creek (pink). Rozet (blue) has different properties that cause slower and lower porosity than the rest of the Muddy. Octagon: C well; square: G well; triangle: A well. Vp and Vs represent the velocity conditions after replacing any oil saturation with brine by fluid saturation.

The relationship between density and velocity in the Bell Creek reservoir is complex. In general, Vp increases, and Vs decreases as clay volume increases. Moreover, high clay volume samples have higher densities and lower velocities. The increase of bulk modulus and decrease in shear modulus with an increase in volume of clay (Vclay < 0.3) are much less apparent than it is with velocity. Therefore, it can be assumed that the change in velocity is mostly density-driven.

### 4.3 Rock physics analysis and diagnostics

Rock physics analysis and diagnostics are used to relate seismic characteristics to geology. The connection can be observed by plotting thin-section images from cores relative to their log properties. The results can provide a useful reference for the rock physics analysis. Fig. 9 shows thin sections from C well on a Vp vs. density porosity (DPHI) plot of the A (triangles), C (circles), and G (squares) wells from the reservoir section colored by clay volume. The thin sections'

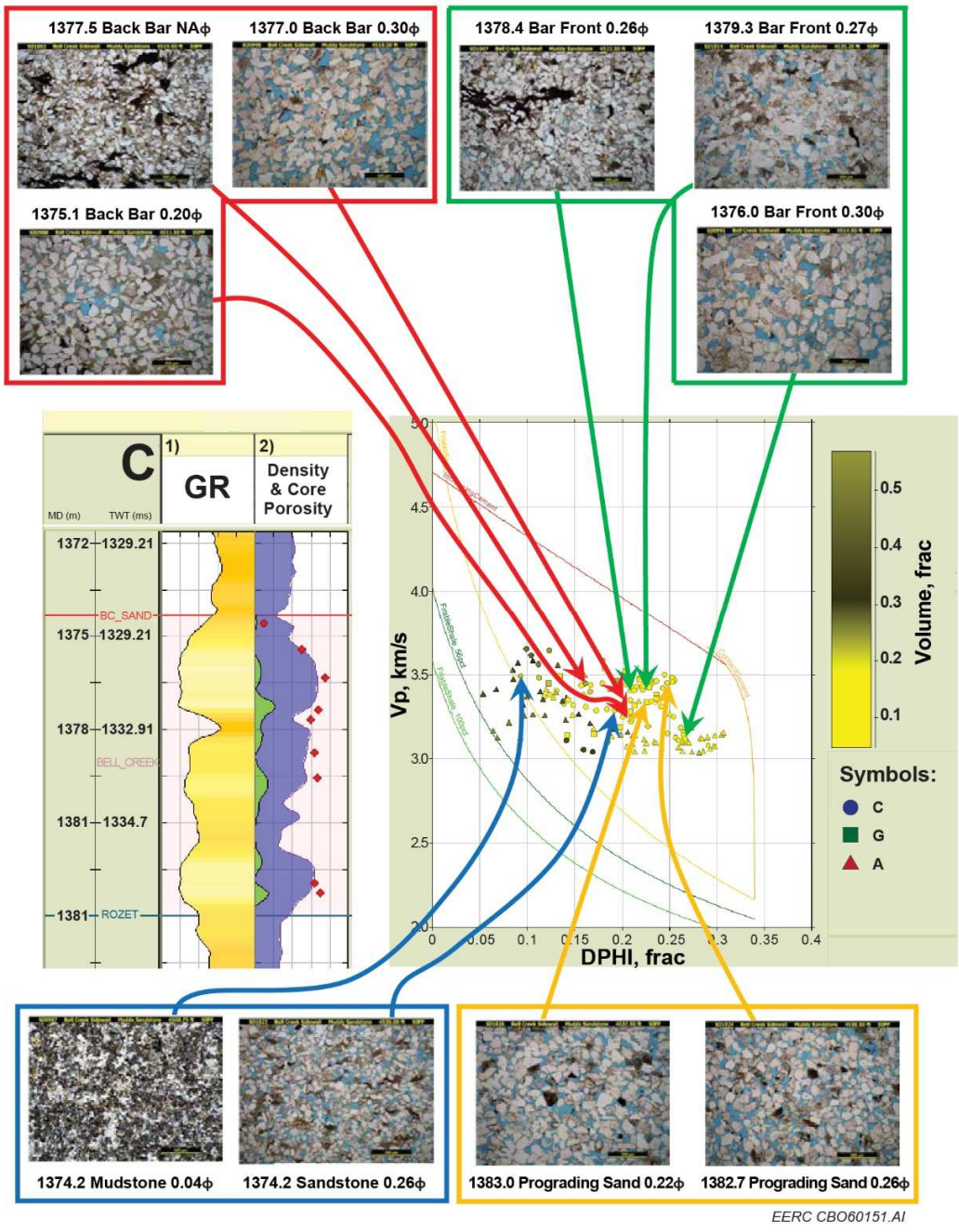


**Figure 9**. Core data from Bell Creek reservoir at the C well are placed on a Vp (wet) vs. density porosity (DPHI) plot colored by clay volume with data from A (triangles), C (circles), and G (squares) wells. The curves represent the effective medium models: contact cement (dark orange), friable sand (yellow orange), increasing cement (red brown), friable shale 56% (clay) (dark green), and friable shale 100% (clay) (bright green). The depth (m), the interpreted facies labels of the core plug, and core porosity are located below and at the side of the thin section.

porosity measurements, core measurements, and Vp measurements were obtained from the correlation with the log measurements as discussed above. Notice that the bar front and prograding sand facies have the highest porosities for their Vp, followed by the back bar facies and the nonreservoir facies. The loss of porosity is consistent with decaying sorting, where the bar front and prograding sand facies are best sorted, followed by the back bar facies. As expected, Vp increases as porosity decreases.

Diagnostic rock physics models are used to relate seismic and elastic properties of the reservoir and the surrounding formations to geologic observations. They can facilitate predictions of seismic properties away from the wells that are created by stratigraphic conditions and fluid saturations that have not yet been encountered by drilling or in outcrops. A well-calibrated model may be used to predict geologic properties, away from well control.

When rock physics diagnostic models fit Vp and porosity, they often predict Vs, bulk, and shear moduli poorly. Granular rocks often have lower shear modulus than expected from the models, possibly as a result of some grain contacts that do not slip under compression, do slip under shear. Since Vp involves both moduli, fitting a model to Vp alone often results in an underprediction of bulk modulus and an overprediction of shear modulus and associated Vs. An ad hoc shear reduction factor was used in this study to represent grain slip and to improve the model fitting. One of the problems with the shear reduction factor is that it changes the entire model's shear components, including the well-defined values at the mineral points. The models used in this study were fitted in the moduli space to better constrain the shear reduction factor and to obtain an improved estimate of the bulk modulus. Following this approach, it was possible to fit the bulk modulus and then adjust the shear reduction factor to fit the shear modulus. Then,

fitting Vp and Vs only required adjusting the density model. Additionally, the model fitting was tested in Vp/Vs vs. AI space.

Several rock physics models were used in the rock physics diagnostic analysis of the Bell Creek reservoir. The following is a brief description of the models; more detail can be found in Avseth et al. (2005):

- Friable sand: models the elastic properties of uncemented sand as sorting changes and porosity is lost. The high-porosity well-sorted endpoint is defined by the Hertz–Mindlin theory, and the poorly sorted endpoint is defined by the mineral properties. The endpoints are connected by a modified Hashin–Shtrikman lower bound (Dvorkin and Nur, 1996).
- Friable shale: same as friable sand except that it is used to model changes in elastic properties of a constant mixture of sand and clay as sorting changes and porosity is lost.
- Contact cement: models the effect of initial cementation at grain contacts of a high-porosity grain pack. The model is only valid at high porosity and for small volumes of cement. The model is numerical, and the details are given in Dvorkin et al. (1994).
- Increasing cement: models the effect of increasing cement volumes above those modeled by the contact cement model. It is valid for intermediate cement volumes. The porosity limits are interpretive. The high-porosity endpoint is the intersection with the contact cement model, and the low-porosity endpoint is defined by a effective elastic properties of a mixture of sand grains and porosity-filling cement. The endpoints are connected by a modified Hashin–Shtrikman upper bound (Avseth et al., 2005).
- Constant cement: like the friable sand model, except here, the high-porosity well-sorted endpoint is defined by the contact cement model. The volume of cement is held constant as porosity decreases and sorting decays (Avseth et al., 2000).

A composite framework model resulting from the combination of the friable sand, friable shale, contact cement, and increasing cement models was used to assess the volume of cement and shale properties of the Bell Creek reservoir, as shown in Fig. 10.

The Bell Creek reservoir is a mixture of shaley sand and sandy shale deposited in a barrier bar–strand plain sedimentary environment. The reservoir facies are relatively thin and complicated by the vertical and lateral variability of the depositional environment. This combination of factors creates inconsistency in porosity, sorting, and clay content, all of which influence the rocks' elastic properties.

Marion et al. (1992) developed a model to explain changes of elastic properties of unconsolidated mixtures of sand and dispersed clay as the mixtures are varied. The model was extended to consolidated mixtures measured with wireline logs by Dvorkin and Gutierrez (2002). This model starts from clean sand and adds porous clay to the pore space until filled without disturbing the grain contacts. This point is called the critical clay volume. If more clay is added, then sand must be removed, and the grains begin to separate. More clay is added, and sand removed until the sample is 100% clay. The critical clay volume marks the transition from grain-supported shaley sand to matrix-supported sandy shale.

From Marion et al. (1992) and Dvorkin and Gutierrez (2002) models, it can be inferred that Vp increases, and porosity decreases as clay fills the pore space, replacing fluid until critical clay volume is reached. When clay volumes are greater than critical clay volume, porosity increases, and Vp decreases. The porosity increase is due to nonporous quartz being replaced with porous clay. Vp decreases as clay volumes become greater than the clay full point because of the replacement of high-velocity quartz with lower-velocity clay.

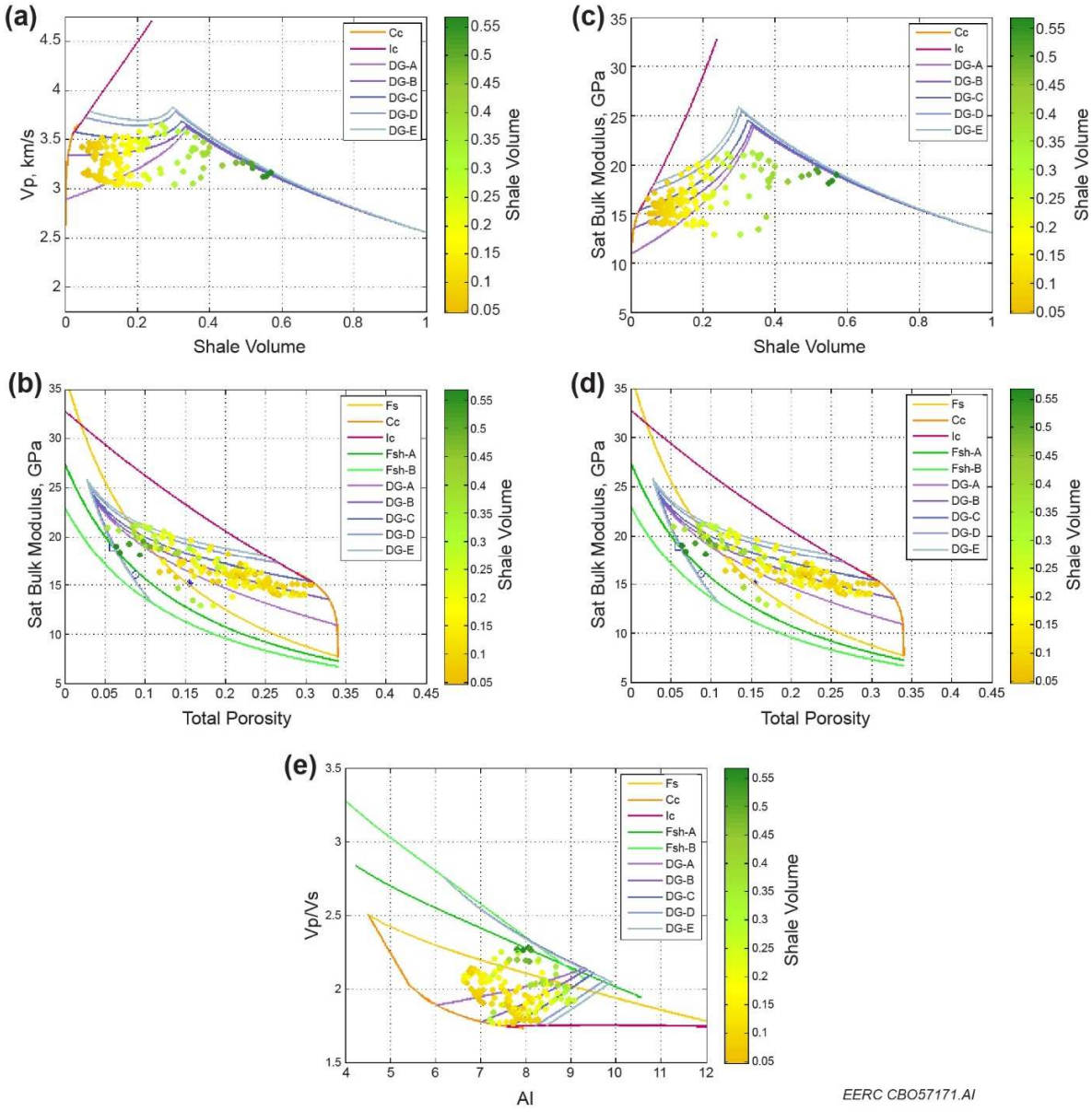


**Figure 10**. Rock physics diagnostic Dvorkin–Gutierrez and framework models a) Vp vs. shale volume (Vshale); b) Vp vs. total porosity (Phit); c) bulk modulus vs. Vshale; d) bulk modulus vs. Phit; e) Vp/Vs vs. AI, where the models are Fs – friable sand, Cc – contact cement, Ic – increasing cement, Fsh-A – friable shale with 0.56 clay and 0.44 quartz, Fsh-B – friable shale with 1.0 clay, Dvorkin–Gutierrez shaley sand models DG-A – cement volume 0.001, DG-B – cement volume 0.011, DG-C – cement volume 0.035, DG-D – cement volume 0.075, DG-E – cement volume 0.092. Estimated shale properties from Table 1: blue square – Bell Creek, blue circle – Rozet, and blue asterisk – Springen Ranch.

| | Vp, km/s | Vs, km/s | Density, g/cm$^3$ | K, GPa | Mu, GPa | DPHI, frac |
|---|---|---|---|---|---|---|
| Bell Creek | 3.18 | 1.39 | 2.52 | 18.9 | 4.9 | 0.06 |
| Springen Ranch | 3.07 | 1.53 | 2.40 | 15.2 | 5.59 | 0.155 |
| Rozet | 2.93 | 1.27 | 2.51 | 16.1 | 4.07 | 0.09 |

**Table 1**. Shale properties in the C well for Springen Ranch, Bell Creek, and Rozet based on well log data. K: bulk modulus and Mu: shear modulus.

The Dvorkin and Gutierrez (2002) model was applied to the Bell Creek and Springen Ranch to find the critical clay volume, which is identified as the point in a sand–clay mixture where Vp is maximum. (Fig. 10). Maximum Vp (3.652 km/s) occurs at a volume of 0.267 dry clay. This is in the range expected for critical clay volume (the critical clay volume is generally between 0.2 and 0.4 volume clay). Density porosity is 0.1 at the critical clay volume. When converted to a total volume, the critical clay volume including clay porosity is 0.34. This value is close to the maximum density porosity in the Bell Creek, which is 0.31 in the A well with 0.05 volume clay. When converted to total volume with the clay removed, a clean sand porosity of 0.34 is estimated, which agrees with the critical clay volume. The critical porosity for clean sand is likely to be close to 0.34, which supports the hypothetical clean sand critical porosity used in the rock physics models. In general, the data show much variability in Vp for any given volume of clay. This variability could be explained by a changing depositional environment causing changes in sorting and clay's contribution to the elastic properties. Some of the clays are likely in laminated sands, and others may be in the contact between sand grains. In both cases, Vp is low relative to a grain pack with dispersed clay. Variation in the volume of contact cement may also contribute to the variability. Changes in clay physical properties between Rozet and Springen Ranch could also add to the variability.

The following parameters were used to produce the Dvorkin–Gutierrez models shown in Fig. 10: Dvorkin–Gutierrez shaley sand, sand endpoints, DG-A – intersects contact cement model

544 at 0.001 volume cement, DG-B – intersects contact cement model at 0.011 volume cement, DG-C
545 – intersects increasing cement model at 0.035 volume cement, DG-D – intersects increasing
546 cement model at 0.075 volume cement, and DG-E – intersects increasing cement model at
547 0.092 volume cement.

548 Although the standard practice is to parameterize the model based on the cleanest sand and
549 shaliest shale, poor results were obtained with this parameterization. Therefore, the contact,
550 cement, or increasing cement model for properties of the sand and the friable shale model at 100%
551 clay for the shale properties were used for the model parameterization and iterated to find the shale
552 porosity that fit the data. The models derived with these properties in Fig. 10 are consistent with
553 the observations. The sandy shale model produces a trend that passes close to markers for the Bell
554 Creek and Rozet shales' average properties. Although individual models in Fig. 10 are challenging
555 to identify in the observations, the upper limit of the models appears to conform to the upper limit
556 of the data when plotted on bulk modulus vs. clay and Vp vs. clay volume plots. The sandy shale
557 portion of the model fits best when clay porosity is 0.11.

558 The depositional complexity reflected in the wide variation of sand porosity may create
559 variation in the elastic properties, leading to uncertainty in the critical clay volume. Variation in
560 clay grain properties and porosity may also contribute. The depositional environment changes from
561 nearshore to barrier bar, to lagoon, to onshore; in some cases, the deposition style (e.g., laminated
562 deposits) is inconsistent with the model's assumptions. Given this complexity, it is likely that there
563 is more than one critical clay volume. Finally, a potential second shale trend is observed in the
564 bulk modulus vs. clay volume plot in Fig. 10 but not in the Vp vs. clay volume; thus, a second
565 higher-porosity shale trend potentially related to the Springen Ranch is suspected.

## 4.4 Pressure sensitivity

Time-lapse seismic measurements are primarily affected by changes in reservoir pore pressure and fluid saturation (e.g., Landrø, 2001; Lumley, D., 2010). Rock physics modeling was conducted to estimate the pressure and saturation scenarios of the Bell Creek reservoir. Reservoir and fluid properties obtained from petrophysics, geology, and reservoir simulation were used for the pressure and fluid substitution modeling.

Since neither laboratory measurements of Vp and Vs on dry rocks of the Bell Creek nor an analogous set of measurements from an area with similar geology and structural history were available, the MacBeth (2004) empirical model was used to predict the pressure sensitivity for the Bell Creek reservoir. Pressure response data are typically limited to the reservoir's permeable parts; therefore, the model's application was limited to the Bell Creek's sandy facies.

The stress sensitivity relations from the MacBeth model are based on laboratory measurements on rocks over a wide range of conditions. The model is given for $K_{Dry}$ and $\mu_{Dry}$ for effective pressure ($P_{eff}$) as follows:

$$K_{Dry} = \frac{K_{\infty}}{1 + \left(\frac{S_k}{(1-S_k)}\right) e^{\left(\frac{-P_{eff}}{P_k}\right)}} \tag{2}$$

$$\mu_{Dry} = \frac{\mu_{\infty}}{1 + \left(\frac{S_{\mu}}{(1-S_{\mu})}\right) e^{\left(\frac{-P_{eff}}{P_{\mu}}\right)}} \tag{3}$$

This model requires knowledge of the average porosity, initial and final pore pressures, and overburden pressure. Average porosity is the only parameter required to determine model coefficients from MacBeth (2004) pressure sensitivity crossplots. The Bell Creek average porosity was derived from histograms of density porosity in the reservoir's sandy facies at the A, C, and G wells. The estimated average porosity of 23% was used to derive the following MacBeth model

parameters: total stress for bulk modulus ($S_\kappa$) = 0.59; pressure constant for bulk modulus ($P_\kappa$) = 6 MPa; highest-pressure asymptote for bulk modulus($\kappa_\infty$) = 12.4 MPa; total stress sensitivity for shear modulus ($S_\mu$) = 0.59; pressure constant for shear modulus ($P_\mu$) = 7 MPa, and highest-pressure asymptote for shear modulus($\mu_\infty$) = 10.9 GPa.

An overburden pressure of 30.19–30.42 MPa was calculated by integrating a density log from the C well between the surface and reservoir, assuming a density of 2.07 g/cm$^3$ between the top of the log and the surface. A value of 30.33 MPa was adopted for the overburden pressure of the Bell Creek reservoir.

Pore pressure estimation is complicated because pressure values were required when the well was drilled and when each seismic survey was acquired. Pore pressure can be derived from wireline formation testers, drill stem tests, production data, or reservoir modeling. As pore pressure data for individual wells at Bell Creek were not available, average values from the reservoir simulation were used.

The available data are discussed below:

- As described in Fig. 11, the C well was drilled and logged in December 2012, which is between acquisitions of baseline and monitor seismic surveys. Pore pressure at the time of the baseline survey was 3.75 MPa lower than when C well was logged. Pore pressure at the time of the monitor survey was 1.91 MPa higher than when C well was logged.
- The G and A wells were drilled and logged in March 2013, which is between the acquisition of the baseline and monitor seismic surveys. Pore pressure at the time of the monitor survey was 3.89 MPa lower than when G and A wells were logged. Pore pressure at the time of the monitor survey was 1.86 MPa higher than when the wells were logged.

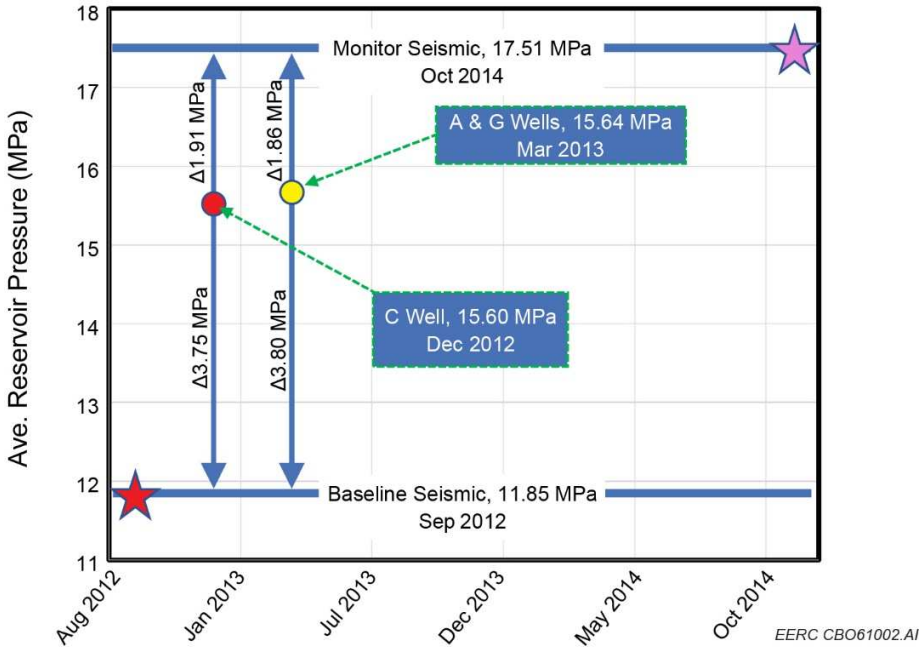


**Figure 11**. Average reservoir pressure conditions during the time-lapse seismic surface survey. Red star: baseline seismic surface survey (11.85MPa in September 012); pink star: monitor seismic surface survey (17.51 MPa in October 2014); red circle: C well (15.60 MPa in December 2012); A and G wells (15.64 MPa in March 2013).

The pressure substitution based on MacBeth's relationships used here involves a combination of fluid substitution to remove fluid effects and pressure substitution applied to the dry matrix and resubstituting of the fluids modeled at the new pore pressure back into the rock. Therefore, the rocks in the model were fluid-substituted to wet before pressure substitution. In general, increasing pore pressure should cause Vp and Vs to decrease. The application of the model to the Bell Creek reservoir produces the results shown in Fig. 12. The velocities in all three wells are influenced by pore pressure changes. Whereas the pore pressure at the time of the baseline seismic survey was lower (green curves) and Vp and Vs were higher than when the wells were drilled, the pore pressure at the time of the seismic monitor survey was higher (pink curves), and velocities were lower.

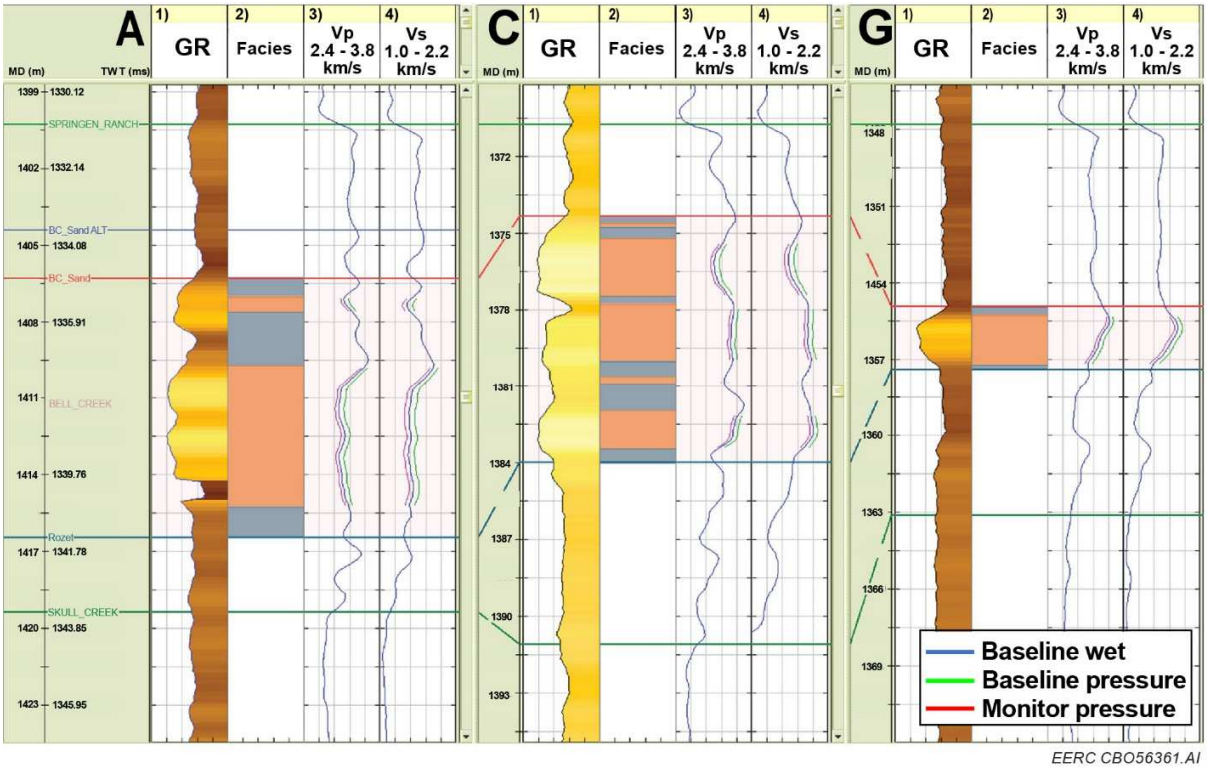


**Figure 12**. Results of pressure sensitivity modeling for A, C, and G wells. Left to right tracks at each well: GR, facies (orange: sandy, gray: shaley), Vp, and Vs. Blue curves: original water-saturated Vp and Vs.; green curves: baseline survey; pink curves: monitor survey.

## 4.5 Fluid properties and substitution

Prasad et al. (2021) provide an excellent discussion on fluid the challenges associated with the standard fluid substitution using the Gassmann approach for $CO_2$ storage projects as part of the seismic inversion workflow. Prasad et al. (2021) report the significant changes in rock properties due to $CO_2$ injection and the time-lapse seismic signatures associated with those changes. Prasad and coauthors emphasize the importance of developing rock physics models to assess second-and third-order changes in seismic properties throughout laboratory studies, small-scale field pilots, and monitoring large-scale geologic storage of $CO_2$.

Diagnostic analysis of rock properties and the effects of fluid saturation changes require that the reservoir in all the wells has the same initial fluid saturation. Gassmann's equations (1951) were used for fluid substitution from in situ to brine-filled conditions. The equations require information on initial fluid saturation, fluid elastic properties, rock elastic properties, and total porosity.

$$\frac{K_{Sat}}{K_{Mineral}-K_{Sat}} = \frac{K_{Dry}}{K_{Mineral}-K_{Dry}} + \frac{K_{Fluid}}{\varphi(K_{Mineral}-K_{Fluid})} \quad (4)$$

$$\mu_{Sat} = \mu_{Dry} \quad (5)$$

where $K_{Sat}$ is the effective bulk modulus of the rock with pore fluid, $K_{Mineral}$ is the bulk modulus of mineral material making up the rock, $K_{Dry}$ is the effective bulk modulus of dry rock, $K_{Fluid}$ is the effective bulk modulus of pore fluid, $\varphi$ is the porosity, $\mu_{Sat}$ is the effective shear modulus of rock with pore fluid, and $\mu_{Dry}$ is the effective shear modulus of dry rock.

Initial fluid saturation was obtained from the Schlumberger RST Advisor analysis of the wireline and baseline pulsed-neutron logs (PNL). Fluid properties for in situ oil and brine were obtained from measurements on produced fluids. Rock composition was obtained from Schlumberger RST SpectroLith analysis. Grain bulk modulus was calculated using standard properties and Voigt–Reuss–Hill average (Mavko et al., 2009). Porosity is based on density porosity on a sandstone matrix.

### 4.6 Elastic properties of fluids and their mixtures

Modeling of elastic fluid properties is critical to the quantitative time-lapse analysis of the Bell Creek reservoir. Table 2 provides an overview of reservoir and fluid properties used for fluid substitution modeling. The reservoir temperature and pore pressure indicate that $CO_2$ will be

| Muddy Reservoir | Baseline Seismic Sep 2012 | Well C Dec 2012 | Wells A and G Mar 2013 | Monitor Seismic Oct 2014 |
|---|---|---|---|---|
| Temperature, °C | 42.2 | 42.2 | 42.2 | 42.2 |
| Ave Pore Pressure, MPa | 11.84 @ Well C | 15.60 @ Well C | 15.64 @ Well C | 17.51 @ Well C |
| Pore Pressure Range (Inj/Prod), MPa | 18.62/12.41 | 18.62/12.41 | 18.62/12.41 | 22.75/16.55 |
| Brine Salinity, mg/L | 6013 | 6013 | 6013 | 6013 |
| Oil GOR, $m^3/m^3$ | 2 | 2 | 2 | 31 |
| Oil API | 37.8 | 37.8 | 37.6 | 33.1 |
| Gas Gravity | 0.83 | 0.84 | 0.84 | 2.18 |

**Table 2.** Reservoir and fluid properties for the Bell Creek, Muddy reservoir. The changes in oil properties in October 2014 are due to the presence of $CO_2$.

supercritical. The Fluid Acoustics for Geophysics (FLAG) modeling algorithm (Han and Batzle, 2014) was used to model the elastic properties of brine, dead oil, and supercritical $CO_2$ ($sCO_2$). The FLAG model is designed to work with mixtures of hydrocarbons and water, and mixtures containing $sCO_2$ act differently, thus alternative models are required for mixtures containing $sCO_2$. Models of $sCO_2$-saturated oil and water were built from relationships from the literature; mixtures of oil saturated with $sCO_2$ were modeled using Han et al. (2012) equations; the water saturated with $sCO_2$ was modeled using Han and Sun (2013) equations. All models above are empirical and based on fitting laboratory measurements of Vp and density of defined fluid mixtures under controlled temperature and pressure conditions.

Fig. 13 shows the model results. Notice the following at the zero-water saturation endpoint: Water and water saturated with $CO_2$ (gas-water ratio [GWR] = 26.9) have very similar properties; dead oil is the second highest Vp fluid. Saturation with $CO_2$ lowers its velocity significantly and slightly increases its density, and $CO_2$ at reservoir conditions has the lowest velocity and density.

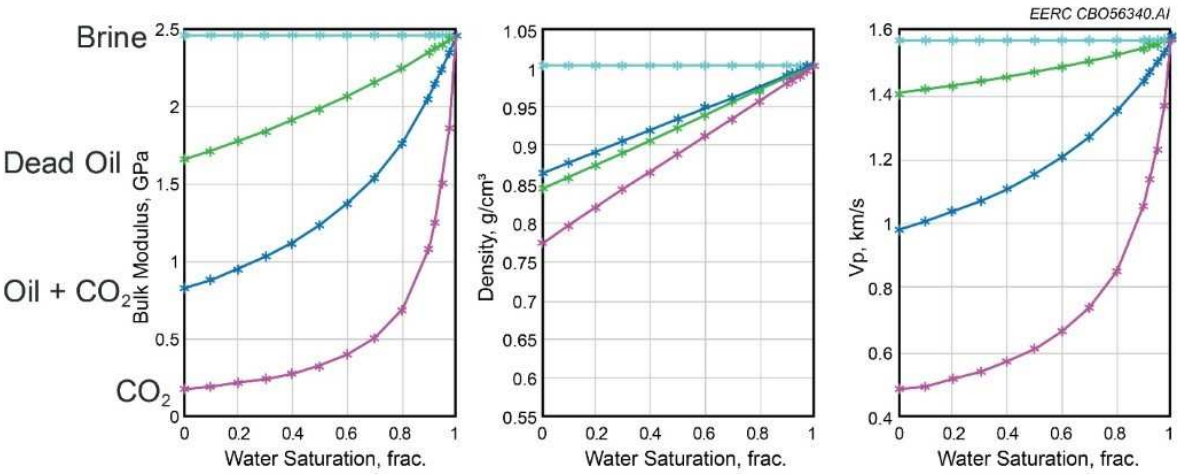


680

681 **Figure 13**. Modeling results of elastic properties of fluids and their mixtures. October 2014
682 fluids mixed with water using Wood's equation. Initial water saturation before EOR is 0.5–
683 0.6 and decreases to an average of 0.35 after EOR. Approximate irreducible water
684 saturation for Bell Creek is Swirr = 0.25.

685

686 Any fluid other than water is unlikely to exist in the reservoir at 100% saturation; other fluids
687 exist as mixtures primarily with water. Using Wood's (1941) equation to describe uniform mixing
688 of fluids in Fig. 13, it is observed that as water saturation increases, the fluid properties converge
689 toward water. Expected water saturations are between an irreducible water saturation of 0.25 and
690 approximately 0.5–0.6, which is the approximate saturation after waterflooding and before $CO_2$
691 EOR. The water saturation after $CO_2$ EOR is expected to be near 0.35.

692 Uniform fluid mixing (Wood's equation) was selected to calculate the bulk modulus of the
693 fluid mixtures used in the inversion. The mixture of $CO_2$-saturated brine with free $CO_2$ is likely to
694 exhibit partial saturation. The amount of partial saturation is expected to vary within the reservoir
695 due to varying geologic properties and reservoir conditions imposed by $CO_2$ injection and oil
696 production processes. It is worth mentioning that using uniform mixing for free $CO_2$ with $CO_2$-
697 saturated brine may lead Ji-Fi to misestimate the free $CO_2$ fluid facies distribution.

698 Domenico (1976) performed lab experiments on unconsolidated sand samples saturated with
699 gas–brine mixtures to determine the effects of changing fluid saturations on P-wave velocity. He
700 determined that uniform fluid mixing best described his results. Most immiscible fluid mixtures
701 are not uniformly mixed. Fluids distribution is controlled by the reservoir rock's microtexture and
702 the relative permeability of the fluids, among many other factors. The separation of a binary
703 mixture into distinct components will cause the equivalent fluid to approximate a Voigt average.
704 Most fluid mixtures have behaviors between these bounds. Brie et al. (1995) proposed an empirical
705 relationship for the behavior of gas–brine mixtures observed in well log data.

706 $$K_f = S_w^e\left(K_w - K_g\right) + K_g \quad (6)$$

707 where $K_f$ = fluid bulk modulus, $K_w$ = brine bulk modulus, and $K_g$ = gas bulk modulus. The Brie
708 exponent e is usually between 2 and 5, and when e = 1, Equation 7 is a Voigt equation, and when
709 e = 40, Equation 7 approximates Wood's equation. The value of the Brie exponent is also expected
710 to be sensitive to frequency of the seismic waves.

711 As an alternative to Wood's equation, a value of Brie exponent in the ranges mentioned
712 could have been selected. The choice of an appropriate value is problematic as this project does
713 not have core flood measurements or time-lapse elastic well logs to help guide the selection.

714 **4.7 Fluid substitution and Ji-Fi fluid facies**

715 The fluid properties were used to create end-member fluid models for Ji-Fi inversion
716 (Table 3). The real fluid mixtures are expected to form a continuum; however, Ji-Fi was limited to
717 four fluid facies models. Two fluid mixtures were selected to describe baseline (September 2012)
718 reservoir conditions and four fluid mixtures to describe monitor (October 2014) reservoir
719 conditions. Water saturations of 1.0, 0.55, and 0.35 were selected for the wet reservoir, oil reservoir
720 after waterflood, and reservoir after $CO_2$ EOR, respectively.

The fluid models represent:

- All brine model – areas outside the field or below the oil–water contact (OWC).
- Dead oil and brine – reservoir after water flooding and before $CO_2$ effect (So = 0.45, Sw = 0.55).
- (oil + $CO_2$) and brine – reservoir where EOR is active ($S_{(Oil + CO2)}$ = 0.65, Sw = 0.35).
- (brine + $CO_2$) and $CO_2$ – areas relatively close to the injectors ($S_{(Brine + CO2)}$ = 0.35, $S_{CO2}$ = 0.65).

| • **Baseline (September 2012)** | **Monitor (October 2014)** |
|---|---|
| Brine | Brine |
| Dead oil (So = 0.45) & brine (Sw = 0.55) | Dead oil (So = 0.45) & brine (Sw = 0.55) |
| | Oil + $CO_2$ (S = 0.63) & brine (Sw = 0.35) |
| | Brine + $CO_2$ (S = 0.35) & $CO_2$ ($S_{CO2}$ = 0.65) |

Note: The symbol "&" indicates fluid mixing with Wood's equation while the symbol "+" indicates modeling of $CO_2$ saturated mixtures of oil and $CO_2$ or water and $CO_2$ using the models mentioned in the main text.

**Table 3**. Fluid mixture models for fluid substitution. The (&) symbol indicates fluid mixing with Wood's equation while the (+) symbol indicates modeling with either the oil and $CO_2$ or water and $CO_2$ empirical fluid property models discussed above.

Gassmann (1951)-based fluid substitution was conducted. It consisted of replacing the brine in the Bell Creek sandy facies of the pressure-adjusted baseline and monitor models with fluid properties from the models in Table 3. Gassmann's equations were used with total porosity from density porosity and a rock model consisting of quartz, carbonate, and clay volume fractions. The baseline fluid model and the monitor model are from September 2012 and October 2014, respectively. Fluid substitution is limited to the sandy facies, which was also used in pressure substitution.

Fluid substitution for the baseline case consisted of replacing the water in the water-saturated baseline pressure-substituted model with a mixture of dead oil and water at four wells: A, B, C, and G. A small reduction in Vp and density relative to the brine-saturated model is observed for the mixture of dead oil and brine.

In the fluid substitution for the monitor case, mixtures of dead oil and water, oil + $CO_2$ and water, and $CO_2$ + water and water replaced the water in the water-saturated monitor pressure-substituted model at four wells: A, B, C, and G. The results for C are shown in Fig. 14. Vp and density decrease as brine is replaced with dead oil and brine, oil–$CO_2$ and water, and $CO_2$ and water, respectively.

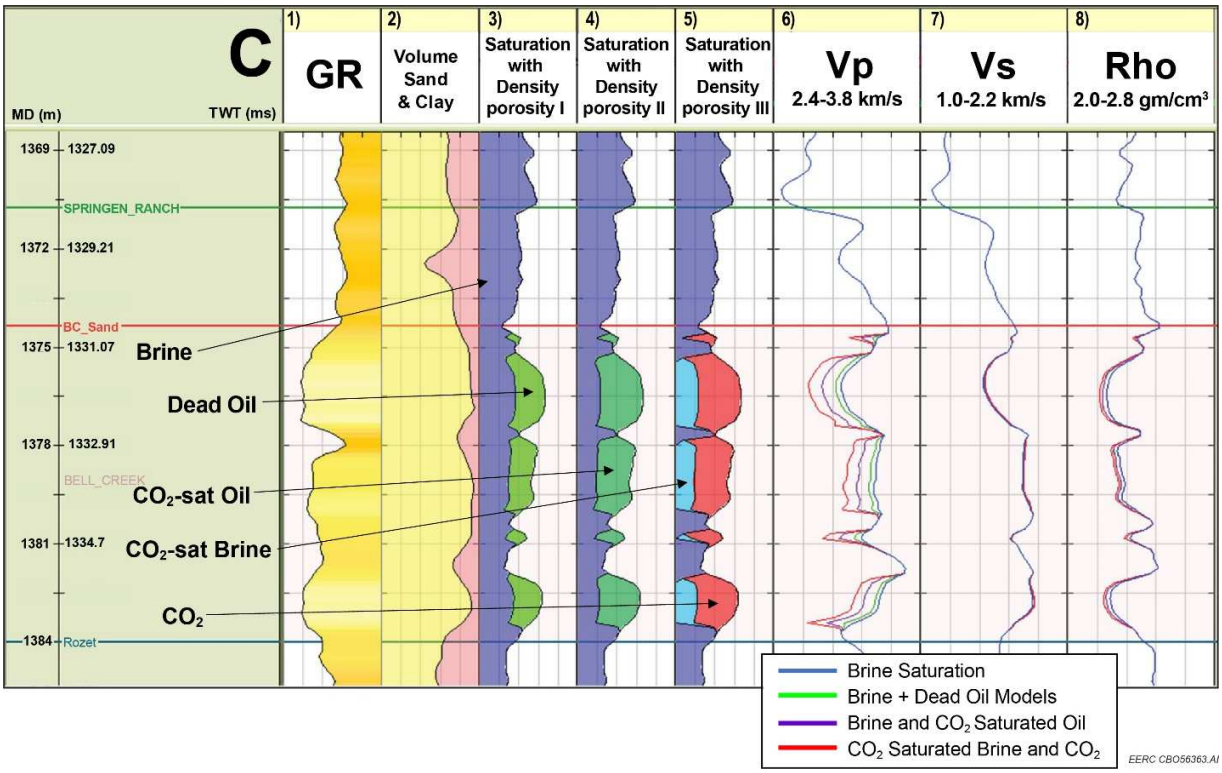


**Figure 14**. Monitor (October 2014) fluid substitution into sandy facies for C well. Left to right tracks: GR, lithology (volume), and three saturations with density porosity (Por Sa) (DPHI) scenarios: 1) brine (dark blue) and dead oil (green), 2) brine (blue) and $CO_2$-saturated oil (dark green), 3) brine (dark blue), $CO_2$-saturated brine (light blue) and supercritical $CO_2$ (red), P-wave velocity (Vp), S-wave velocity (Vs), and density (Rho). Blue curves: 1.0 brine saturation, green curves: brine + dead oil models, purple curve: brine and $CO_2$-saturated oil, red: $CO_2$-saturated brine and $CO_2$.

Baseline and monitor models show a small separation between brine-saturated and dead oil + brine Vp curves. A more significant separation is seen between $CO_2$ + brine, oil + $CO_2$, and dead oil + brine Vp curves, suggesting that the monitor $CO_2$ + brine, $CO_2$ + oil, and unchanged fluid may be easier to separate than the pre-$CO_2$ baseline fluids. Minimal separation is observed for the density curves, suggesting a minimal contribution to amplitude variation with offset (AVO) at very far offsets.

### 4.8 Rock response to change in pore pressure and saturation

The pressure and fluid substitution models can be summarized to show how pressure and saturation changes affect rock properties. When pore pressure is increased from baseline to monitor models, Vp and Vs decrease. When the wet reservoir is replaced with either $CO_2$ + oil or $CO_2$ + water, Vp decreases significantly, and Vs increases slightly because of the fluid's change in density. Hence, saturation change affects Vp, but pore pressure change affects Vp and Vs. The expected percentage of change in Vp for given porosities due to pore pressure and saturation conditions after the $CO_2$ injection into the reservoir in the period of the time-lapse seismic survey are shown in Fig. 15. Inversion results for saturation can have a pore pressure overprint. The wide range of Vp and Vs for such a small porosity range is probably associated with the reservoir's complexity.

## 5. ELASTIC FACIES

Ji-Fi foregoes the traditional method of creating a low-frequency background model separate from a relative impedance inversion. Instead, Ji-Fi combines the two processes into an absolute inversion by constructing the background model iteratively from a set of defined elastic facies and related depth trends. Geologic facies are used to classify rocks according to their appearance or

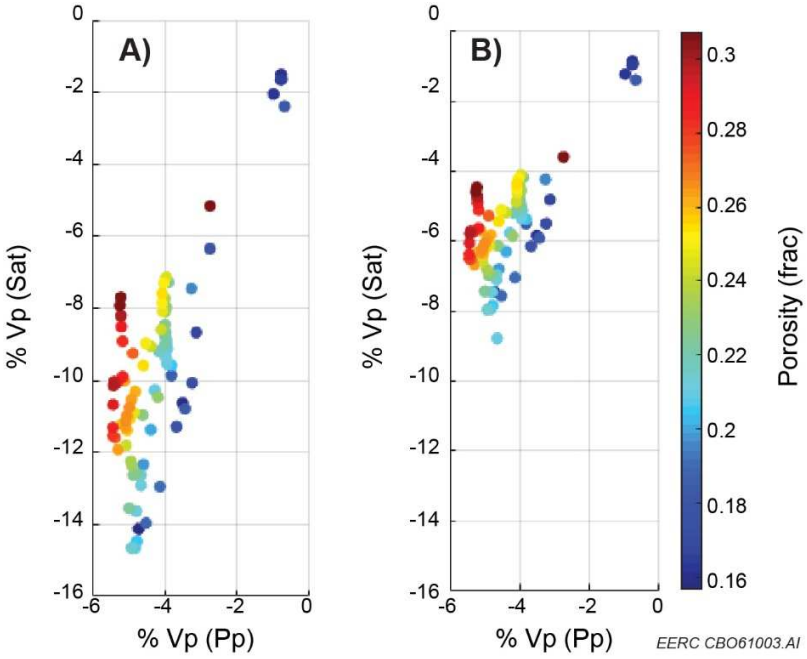


**Figure 15**. Effect of pressure and saturation changes on Vp due to injection of $CO_2$ into the reservoir in the study area: a) percentage of change in Vp between brine saturated and the mixture of brine and $CO_2$ at monitor conditions described in Table 2 (vertical axis) and b) percent change in Vp between brine saturated and the mixture of oil and $CO_2$ at monitor conditions described in Table 2 (vertical axis). The horizontal axis for both figures: percentage of change in Vp due to increasing pore pressure in the period between the baseline and monitor surveys. The dots are colored by porosity.

composition. In Ji-Fi implementation, facies classify rocks based on their shale volume, porosity, and saturation. After creating facies logs from petrophysical logs, an automatic approach that consistently interprets the elastic logs (Vp, Vs, and density) for the facies classification was preferred to minimize the geologic interpretation bias. An unsupervised clustering approach was applied to the elastic logs of the A, B, C, D, E, F, G, and H wells to estimate facies logs without fluids. In this approach, the only initial interpreter intervention is definition of the number of expected facies. The clustering algorithm uses this "hard" constraint in the multidimensional analysis of log data to estimate groups with maximum homogeneity between the groups' elements and the maximum differences between groups. Several iterations were needed to estimate the dry

facies according to the study area geologic conditions (represented by the petrophysical facies logs). In this process, the initial step consisted of analyzing the facies clusters obtained with no prior information on the geology and then relating them to geologic/petrophysical facies. Clustering success is reflected in the separation of the cluster in the seismic (elastic) domain and, therefore, in the quality of the Ji-Fi results.

Since only the reservoir interval corresponding to the Bell Creek sandstone was considered with fluid fill, the litho-fluid facies (facies reflecting not only rock type but also fluid fill) were created according to the fluid substitution modeling cases mentioned in Table 3 (monitor). All of the facies representing the geologic and fluid conditions in the period of the two seismic surveys (September 2012 – October 2014) are shown in Table 4. These facies are integrated into the DTA already explained in a previous section.

| Color | Facies | Type | Comment |
|---|---|---|---|
| | Shallow Marine 1 | Siltstone | |
| | Marine 1 | Shale | |
| | Marine 2 | Shale | |
| | Shell creek | Shale (lagoon, tidal flat) | |
| | Barrier bar | Sandstone (bar) | |
| | Shallow marine intrareservoir | Siltstone (transition) | |
| | Extra shale | Shale | |
| | Shallow Marine 2 | Siltstone | |
| | Marine 3 | Shale (deep sea) | |
| | Barrier bar – dead oil and water | Sandstone (bar) | Fluid substituting |
| | Barrier bar – oil | Sandstone (bar) | Fluid substituting |
| | Barrier bar – $CO_2$ | Sandstone (bar) | Fluid substituting |
| | Barrier bar – water | Sandstone (bar) | Fluid substituting |

Note: The estimated geologic/petrophysical (dry) facies representing the Bell Creek reservoir at different wells are shallow marine intrareservoir, barrier bar, Shallow Marine 2, Marine 3, and Shell Creek. The fluid facies are assigned at the interval representing the Bell Creek sandstone (barrier bar facies). The prefix barrier bar is used in the name of the fluid facies to facilitate the reservoir interval identification.

**Table 4. Facies estimated at the A, B, C, D, E, F, G, and H wells.**

## 6. JI-FI APPLICATION

A DTA was performed to derive per facies relationships between Vp and depth and between Vp, Vs, and density (rho) using the facies derived from the eight wells considered in this project. The per facies background models and the rock physics relationships used in Ji-Fi are derived from the DTA relationships. An example of the DTAs used for the Bell Creek data inversion is shown in Fig. 16. The colored circles represent the trends of each facies derived from well logs at an interval with the highest probability of finding specific facies. The colored crosses (the probability distribution or prior data) complement the rest of the background associated with a specific facies. Notice that in terms of input data for seismic inversion, one facies background model is the equivalent to a low-frequency model in standard model-based inversions.

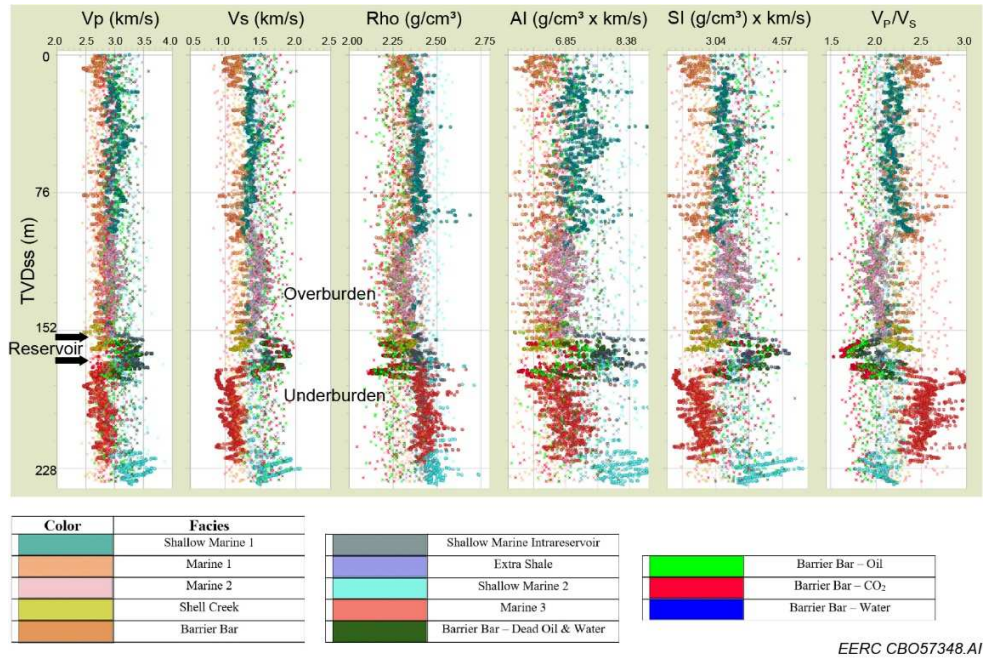


**Figure 16**. Depth trend analysis, including fluid cases used in the Ji-Fi application to the seismic data. Left to right tracks: P-wave velocity (Vp), shear-wave velocity (Vs), density (rho), acoustic impedance (AI), shear impedance (SI), Vp/Vs ratio. Circles: the trend of specific facies at the highest probability interval; cross: prior data (probability distribution) of the specific trend covering the complete inversion interval. The colors of the symbols represent the facies.

The assessment of facies in the depth trends can be simplified when the facies are crossplotted. The trends in Fig. 16 can be studied in crossplots of Vp vs. rho, Vp vs. Vs, AI vs. SI, and AI vs. Vp/Vs ratio with their respective probability distributions shown as ellipses for given standard deviations. Fig. 17 depicts the AI vs. velocity ratio of the reservoir. The circles and ellipses represent the facies' distribution and the probability distribution (one standard deviation), respectively. Note the separation in AI between the Shell Creek (yellow) and shallow marine intrareservoir facies (gray). The separation between the three litho-fluid facies, barrier bar with

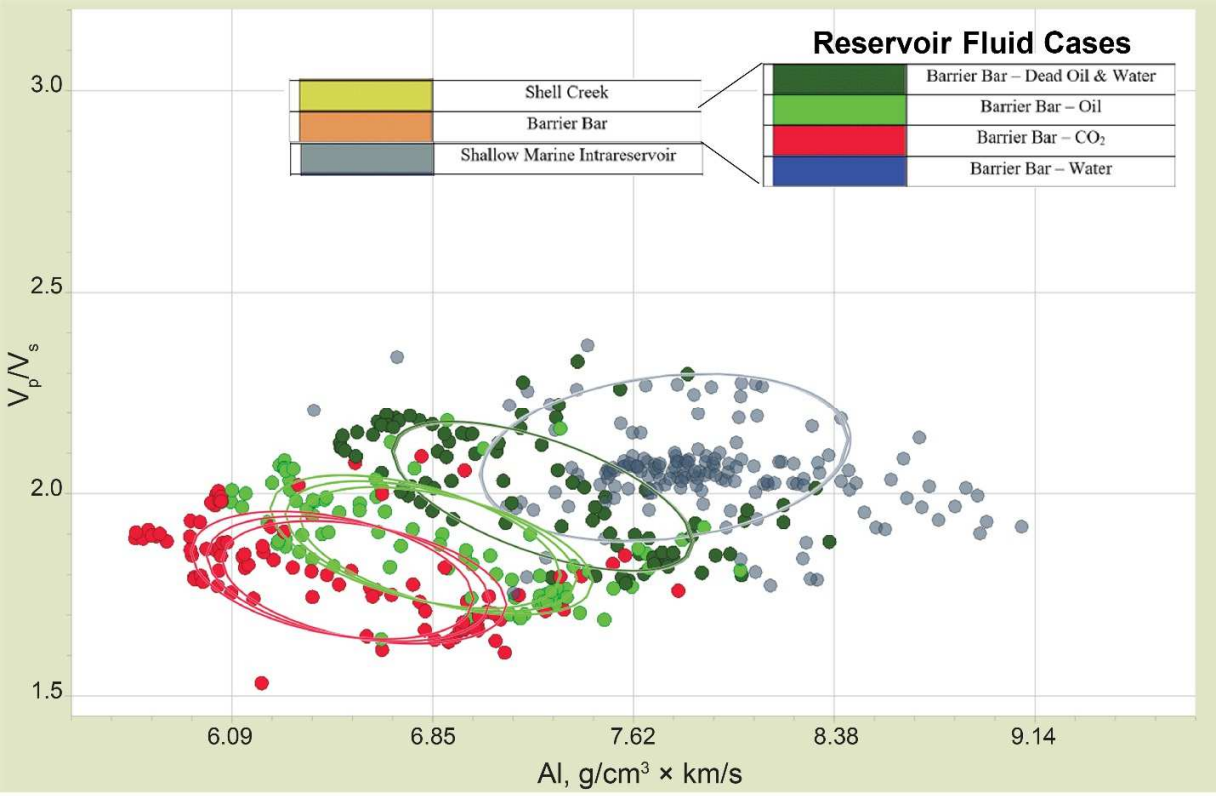


**Figure 17**. AI vs. Vp/Vs crossplot of the DTA shown in Fig. 16(9). Circles: individual facies; ellipses: one standard deviation of prior data (probability distribution). Facies: shallow marine intrareservoir (gray), barrier bar with dead oil and water (dark green), barrier bar with oil (bright green), and barrier bar with $CO_2$ (red).

848 dead oil and water (dark green), barrier bar with oil (bright green), and barrier bar with $CO_2$ (red),
849 is also evident from low AI and low-velocity ratio to high AI and velocity ratio. This type of
850 separation reflects not only the geologic/petrophysical/fluid/seismic characteristics of the reservoir
851 but also the quality of the initial facies estimation. In addition to high-quality input facies, a target
852 zone and an estimation of the proportion of each facies in the target zone are fundamental for
853 running Ji-Fi. The estimation of proportions can be derived from empirical observations generated
854 from previous inversions or reservoir simulations.

855 When the Ji-Fi algorithm is applied to baseline and monitor seismic data sets, each survey
856 is inverted separately. Hence, the time-lapse effect analysis due to changes in fluid conditions in
857 the reservoir is conducted with two sets of impedances and (most probable) facies. This analysis
858 can be simplified when Ji-Fi is applied to arbitrary lines defined through specific interest areas in
859 the seismic cubes. Several arbitrary lines were defined as part of the work developed here. The
860 arbitrary line presented here joins the A, C, D, E, and H wells. Several time-lapse anomalies
861 observed along this line were crucial for refining the Ji-Fi parameters and the fast validation of
862 results.

863 Fig. 18 shows the most probable facies estimated by Ji-Fi for the arbitrary line of the baseline
864 and monitor data sets and the in situ facies (no fluids) at the well locations. The inversion target
865 zone includes the interval between Horizon 1 (top of the target zone) and the LBBC horizon
866 (bottom of target zone). Although the wells are not used as constraints in the Ji-Fi algorithm (as is
867 the case with standard inversions), a good match is observed for the estimated Ji-Fi facies with the
868 facies at wells outside the reservoir. The comparison of in situ (no fluids) from the wells with the
869 litho-fluid facies reflects the fluid facies' distribution in the in situ facies. The changes between
870

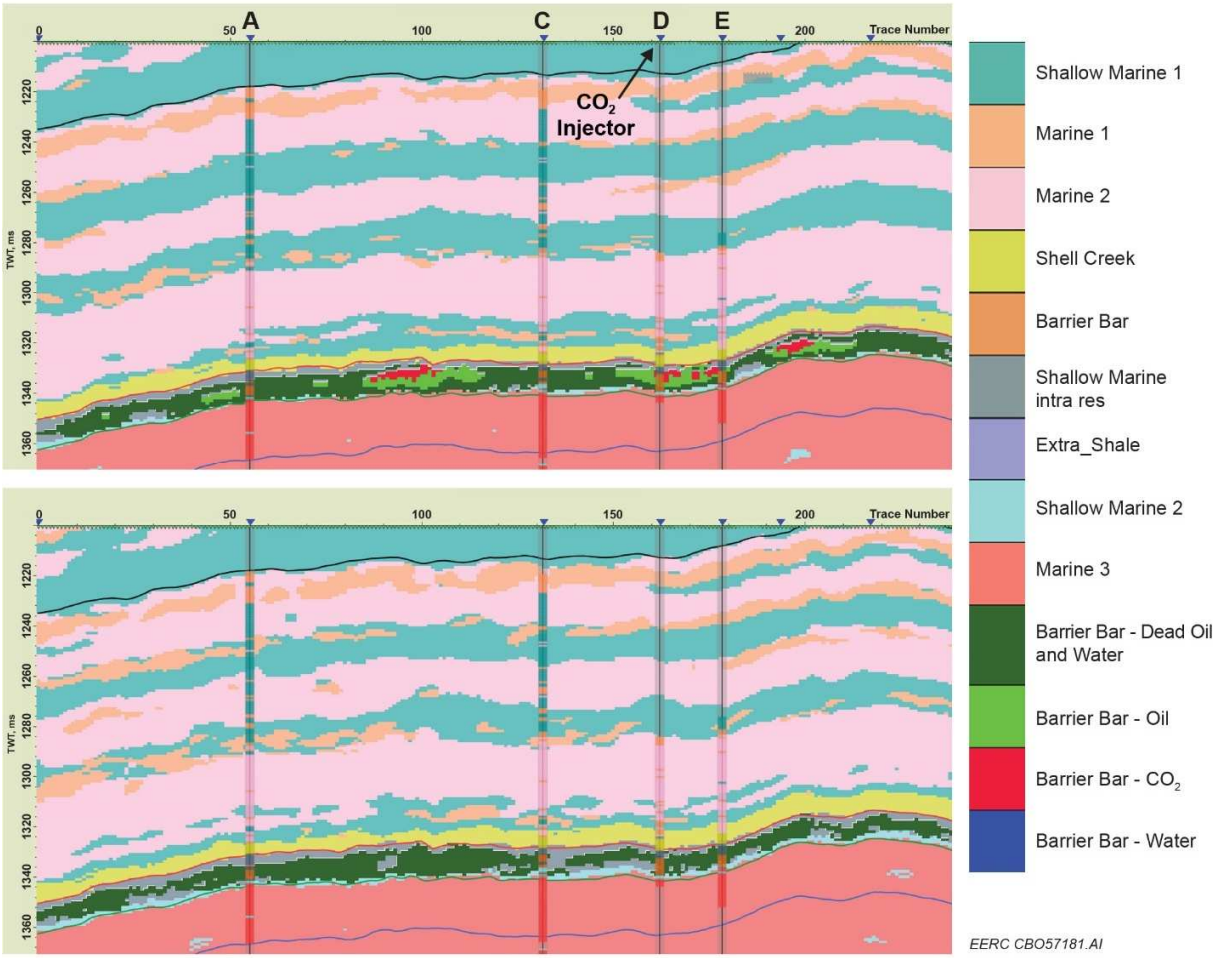


**Figure 18**. Most probable facies estimated by the Ji-Fi algorithm at the arbitrary line for the baseline (bottom) and monitor (top) seismic data sets. The A (producer), C (observation), D ($CO_2$ injector), and E (producer) wells show the estimated in situ facies (no fluids). The seismic inversion shows the results using litho-fluid facies at the reservoir as input. The cross sections do not include the part of the line where the H (dry) well is located.

the reservoir litho-fluid facies from baseline to monitor correctly predict the location of $CO_2$ and oil saturated with $CO_2$ in the profile. These changes are easily seen on the estimated AI and litho-fluid facies derived from the 3D Ji-Fi on a horizon at 6 ms below the top of the reservoir (Fig. 19).

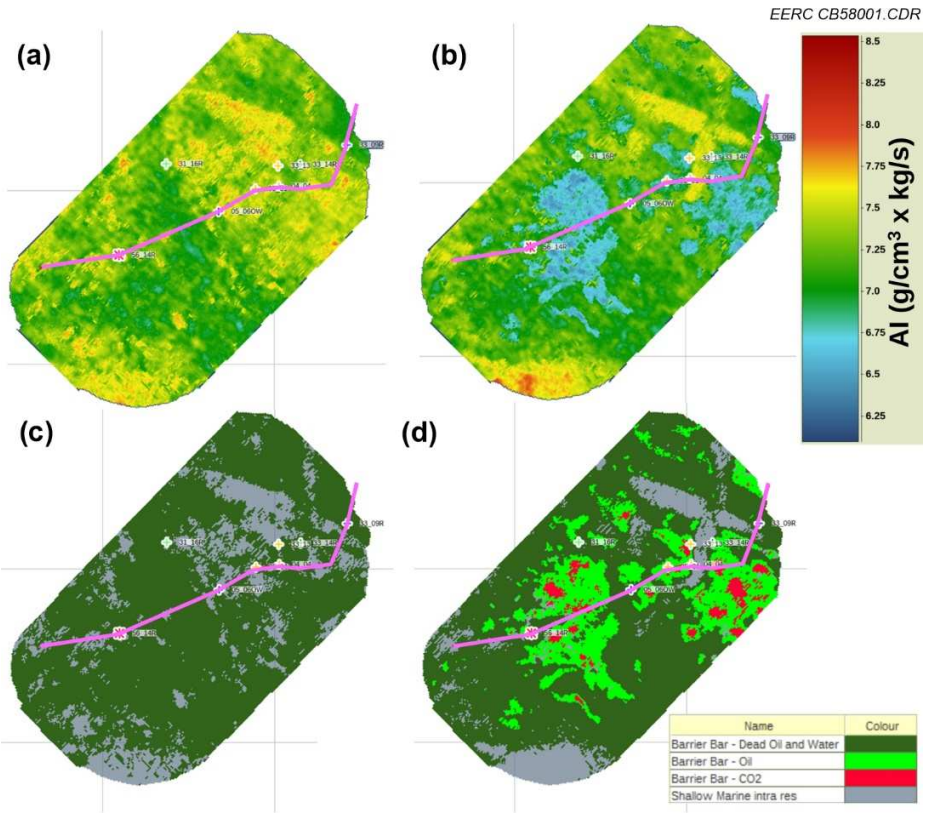


885
886
887 **Figure 19**. Top. AI estimated by Ji-Fi at the reservoir level (6 ms down from the reservoir) for the
888 baseline (left) and monitor (right) seismic data sets. Bottom: Most probable facies estimated by Ji-
889 Fi at the reservoir level (6 ms down from the top of the reservoir) for the baseline (left) and monitor
890 (right) seismic data sets. The symbols (* and +) represent the location of the wells used in this
891 study. The pink line on all the maps represents the location of the arbitrary line shown in
892 Figure 18.
893

894 The good performance of the Ji-Fi algorithm should be noted. The estimated AI decreases
895 (Fig. 19 top) because of reservoir fluids changes in the monitor survey. Several parameterizations
896 of Ji-Fi were tested for the baseline and monitor (not shown here). Combinations of parameters
897 generated some variations in the estimated facies and acoustic impedances. Eight Ji-Fi realizations
898 were combined in a multirealization scheme to estimate the most probable facies and the
899 probabilities of the barrier bar with different fluids.

900

## 7. FLUID DISTRIBUTION FROM JI-FI VS. DISTRIBUTION FROM RESERVOIR SIMULATION

The probabilities of facies fluid distribution in the Bell Creek Reservoir estimated by Ji-Fi are compared here with gas saturation distribution derived from reservoir simulations in Fig. 20. The gas distribution from reservoir simulation corresponds to Layer 11 from October 2014, the same month when the seismic monitor survey was acquired. This layer was selected

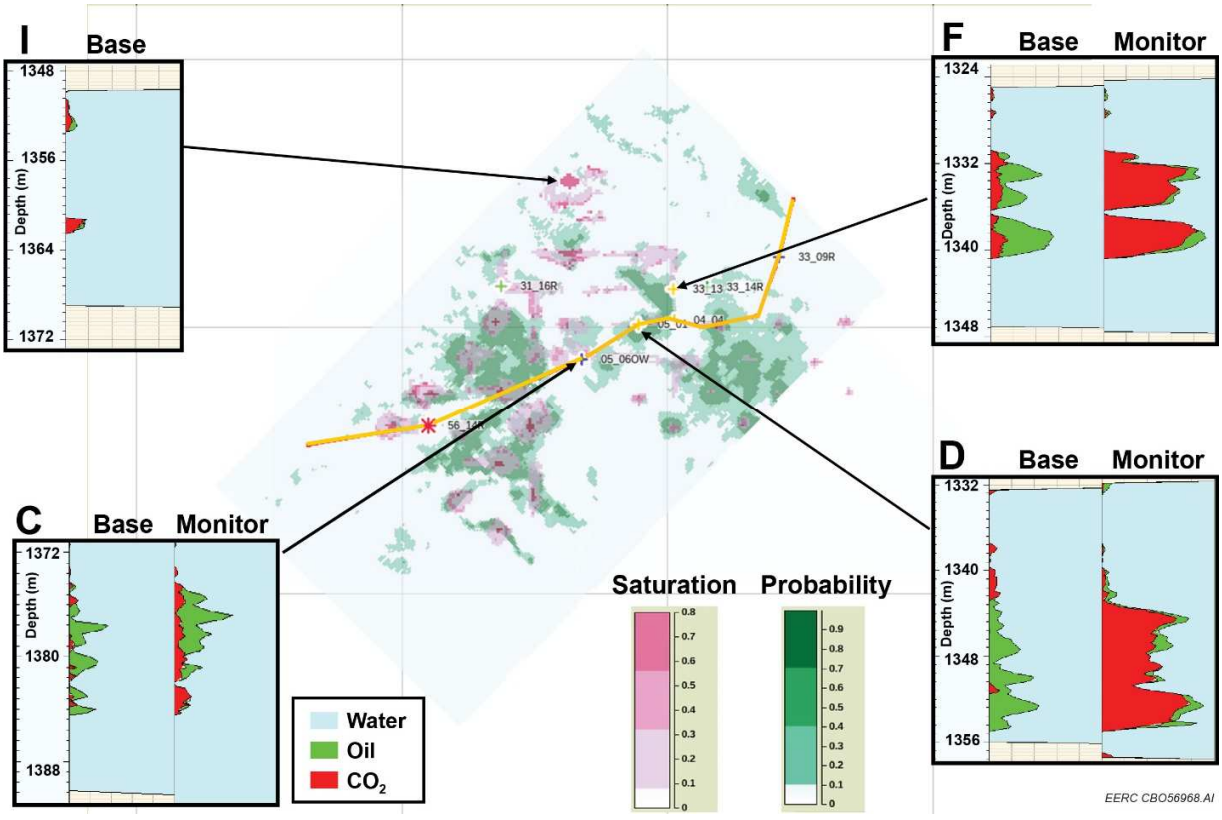


**Figure 20**. Comparison of gas saturation from reservoir simulation results at Layer K11 (October 2014) with estimated probabilities for free $CO_2$ and oil saturated with $CO_2$ using a Ji-Fi multirealization approach. The Ji-Fi results overlay the reservoir simulation results. Green bar: Ji-Fi, pink bar: reservoir simulation. Time-lapse PNL of the C, D, and F wells from the same time of acquisition as the seismic survey. The PNL from the I ($CO_2$ injector) well is only available after the $CO_2$ injection.

because of its location approximately at the middle of the reservoir interval. The Ji-Fi probability fluid distribution is shown by a horizon with the same geometry as the Springen Ranch horizon, representing the reservoir top. The Ji-Fi horizon was placed 6 ms down from the top of the reservoir. It should be noted that although the geometry of Layer 11 and the Ji-Fi horizon are not the same, it was expected that both surfaces cross similar features of the reservoir. Overlaying the Ji-Fi facies probabilities horizon on the gas distribution map for free $CO_2$, oil saturated with $CO_2$, and the combination of free $CO_2$ with oil saturated with $CO_2$ shows a good correlation with the spatial distribution of the gas saturation from reservoir simulation, which confirms the ability of Ji-Fi to detect the changes in fluid saturation conditions in the reservoir due to $CO_2$ injection.

However, some discrepancies in the correlation are observed in the northwestern part of Phase 1. PNLs of some wells in the study area were used to review the geologic and fluid conditions in the reservoir at selected locations and assess the discrepancies. Fig. 20 shows the available PNLs of the C, D, F, and I wells and their location in the Ji-Fi reservoir simulation comparison map. Whereas the PNLs of the D and F-wells show a well-defined saturation in the reservoir, and therefore, a high-probability of reservoir fluids estimated by Ji-Fi, the C and I PNLs show a small saturation area. Only one PNL was available from the I well, where the main discrepancy in the correlation of Ji-Fi versus reservoir simulation was observed. If the small saturation area observed in the PNL is considered a reference for the reservoir's thickness, it is expected that such thickness is below the resolution of the seismic method.

In addition to the saturation effects observed in the reservoir simulation and Ji-Fi comparison, it is expected that some pressure effects are also in the seismic signal. Mur et al. (2020) have reported encouraging initial results of the Ji-Fi application to decouple pressure and

939 fluid effects in the study area. Extending the Ji-Fi method for quantitative pressure detection
940 requires further detailed studies, analysis, and prior conditioning (Mur et al., 2020).

941 **8. CONCLUSIONS**

942 The Ji-Fi method has an integral representation of the geology in the inversion algorithm
943 using elastic facies, which provides information about the spatial distribution of the geologic
944 heterogeneities controlling the distribution of fluids in the reservoir.

945 In this paper, a reservoir properties-focused Ji-Fi workflow was introduced to derive the
946 optimum input data for applying Ji-Fi to the baseline and monitor surveys from the study area.
947 Comprehensive rock physics analyses using core data and well logs were conducted to establish
948 the background geologic information and estimate the Bell Creek reservoir litho-fluid facies. This
949 information was used to create a DTA. Facies model uncertainties were assessed using the facies-
950 dependent probability density functions to perform Bayesian classification along with existing
951 upscaled well elastic data. Good agreement was found between the upscaled petrophysical facies
952 log and the Bayesian classification log with associated probabilities for each facies. The facies and
953 their probability distributions corresponding to the highly heterogeneous target reservoir and its
954 fluid conditions due to the $CO_2$ EOR activities were successfully separated in the seismic elastic
955 space. This separation provided favorable conditions for the application of the Ji-Fi method.

956 Separate Ji-Fi of the baseline and monitor surveys and the differencing analysis to capture
957 changes due to $CO_2$ were performed. Single and multirealization inversion schemes were also run
958 and analyzed. Reliable acoustic impedances and most probably litho-fluid facies of the target
959 reservoir were obtained. Information about the probability of the presence of litho-fluid facies is
960 paramount to reducing uncertainty in forecasting $CO_2$ saturation changes within the target
961 reservoir.

The successful application of the Ji-Fi method to time-lapse seismic data from a mature oil field undergoing $CO_2$ EOR shown in this paper suggests the critical role this type of technology can play in carbon capture, utilization, and storage (CCUS) projects to reduce the uncertainty in the detection and estimation of $CO_2$ distribution.

Since the most common technique to build an LFM (background model) for seismic inversion to estimate absolute elastic rock properties is interpolating well data with a structural and stratigraphic framework (Sams and Carter, 2017), when few wells or no wells are available in CCUS study areas, LFM building can be more problematic.

Estimating relative rock properties without building an LFM is an alternative in such scenarios. A Ji-Fi scheme can also be considered in such well scenarios as the LFM is a product of the inversion, and it is constrained by the elastic property depth trends associated with each expected facies and the inverted distribution of the facies.

The ability to derive the input LFM trends for Ji-Fi from few logs, 1D basin models, or analog fields and incorporate additional information in a Bayesian framework as it is available result in a good seismic inversion alternative.

Future enhancements of the Ji-Fi technology include the simultaneous inversion of the baseline and monitor surveys to relax the time-lapse data acquisition and processing constraints and reduce cost and turnaround time to deliver results to operators and deeper integration of time-lapse seismic inversion with reservoir simulation as suggested by Mur et al. (2020).

## ACKNOWLEDGMENTS

This work was performed under U.S. Department of Energy National Energy Technology Laboratory Award DE-FE0031540. The authors thank Denbury Onshore LLC for providing the

984 data necessary to perform this work and Computer Modelling Group for CMG reservoir simulation
985 software.

986 **REFERENCES**


987 Alnes, H., Eiken, O., and Stenvold, T., 2008, Monitoring gas production and $CO_2$ injection at the
988 Sleipner Field using time-lapse gravimetry: Geophysics, v. 73, no. 6, p. WA155–WA161.

989 Arts, R., Eiken, O., Chadwick, A., Zweigel, P., van der Meer, B., and Kirby, G., 2004, Seismic
990 monitoring at the Sleipner underground $CO_2$ storage site (North Sea): 233, Geological
991 Society London, p. 181–191, Special Publications.

992 Avseth, P., Mukerji, T., and Mavko, G., 2005, Quantitative seismic interpretation—applying rock
993 physics tools to reduce interpretation risk (1st ed.): Cambridge University Press.

994 Avseth, P., Dvorkin, J., Mavko, G., and Rykkje, J., 2000, Rock physics diagnostic of North Sea
995 sands—link between microstructure and seismic properties: Geophysical Research Letters,
996 v. 27, n. 17, p. 2761–2764.

997 Azevedo, L.,Grana, D., and de Figueiredo, L., 2020, Stochastic perturbation optimization for
998 discrete-continuous inverse problems: Geophysics, v. 85, p. M73–M83.

999 Barajas-Olalde, C., Adams, D.C., Kovacevich, J.T., Jin, L., Livers, A.J., Hamling, J.A., Gorecki,
1000 C.D., Cercone, D.P., and Freifeld, B.M., 2020, $CO_2$ injection seismic monitoring without
1001 creating a migrated image, *in* SEG Technical Program Expanded Abstracts: September 25,
1002 2020, p. 71–75, Society of Exploration Geophysicists.

1003 Bhuyian, A.H., Landrø, M., and Johansen, S.E., 2012, 3D CSEM modeling and time-lapse
1004 sensitivity analysis for subsurface $CO_2$ storage: Geophysics, v. 77, no 5, p. E343–E355.

1005 Bosch, M., Mukerji, T., and Gonzalez, E.F., 2010, Seismic inversion for reservoir properties
1006 combining statistical rock physics and geostatistics—a review: Geophysics, v. 75, no. 5,
1007 p. 75A165–75A176.
1008 Bosshart, N.W., Jin, L., Dotzenrod, N.W., Burnison, S.A., Ge, J., He, J., Burton-Kelly, M.E.,
1009 Ayash, S.C., Gorecki, C.D., Hamling, J.A., Steadman, E.N., and Harju, J.A., 2015, Bell
1010 Creek test site—simulation report: Plains $CO_2$ Reduction (PCOR) Partnership Phase III
1011 Task 9 Deliverable D66 (Update 4) for U.S. Department of Energy National Energy
1012 Technology Laboratory Cooperative Agreement No. DE-FC26-05NT42592, EERC
1013 Publication 2016-EERC-10-09, Energy & Environmental Research Center, Grand Forks,
1014 North Dakota, August.
1015 Braunberger, J.R., Pu, H., Gorecki, C.D., Bailey, T.P., Bremer, J.M., Peck, W.D., Gao, P., Ayash,
1016 S.C., Liu, G., Hamling, J.A., Steadman, E.N., and Harju, J.A., 2013, Bell Creek test site –
1017 simulation report: Plains $CO_2$ Reduction (PCOR) Partnership Phase III Task 9 Deliverable
1018 D66 (Update 2) for U.S. Department of Energy National Energy Technology Laboratory
1019 Cooperative Agreement No. DE-FC26-05NT42592, August.
1020 Brie, A., Pampuri, F., Marsala, A.F., and Meazza, O., 1995, Shear sonic interpretation in gas-
1021 bearing sands: SPE 30595, p. 701–710.
1022 Buland, A., and Omre, H., 2003, Bayesian linearized AVO inversion: Geophysics, v. 68, p. 185–
1023 1986.
1024 Burnison, S.A., Bosshart, N.W., Salako, O., Reed, S., Hamling, J.A., and Gorecki, C.D., 2017,
1025 4-D seismic monitoring of injected $CO_2$ enhances geological interpretation, reservoir
1026 simulation, and production operations: Energy Procedia, v. 114, p. 2748–2759.

Burnison, S.A., Burton-Kelly, M.E., Zhang, X., Gorecki, C.D., Steadman, E.N., and Harju, J.A., 2014, Bell Creek test site – 3-D seismic and characterization report: Plains $CO_2$ Reduction (PCOR) Partnership Phase III Task 4 Deliverable D96 for U.S. Department of Energy National Energy Technology Laboratory Cooperative Agreement No. DE-FC26-05NT42592; EERC Publication 2015-EERC-04-04; Energy & Environmental Research Center, Grand Forks, North Dakota, March.

Carrigan, C.R., Yang, X., LaBrecque, D.J., Larsen, D., Freeman, D., Ramirez, A.L., Daily, W., Aines, R., Newmark, D., Friedmann, J., and Hovorka, S., 2013, Electrical resistance tomographic monitoring of $CO_2$ movement deep geologic reservoirs: International Journal of Greenhouse Gas Control, v. 18, p. 401–408.

Chadwick, A., Williams, G., Delepine, N., Clochard, V., Labat, K., Sturton, S., Buddensiek, M., L., Dillen, M., Nickel, N., Lima, A.L., Arts, R., Neele, F., and Rossi, G., 2010, Quantitative analysis of time-lapse seismic monitoring data at the Sleipner $CO_2$ storage operation: The Leading Edge, v. 29, p. 170–177.

Connely, P., 2017, Inversion of seismic data for reservoir properties—recent advances and the road ahead: SEG International Exposition and 87th Annual Meeting.

Davis, T.L., Terrell, M.J., Benson, R.D., Cardona, R., Kendall, R.R., and Winarsky, R., 2003, Multicomponent seismic characterization and monitoring of the $CO_2$ flood at Weyburn Field, Saskatchewan: The Leading Edge, v. 22, p. 696–697.

de Figueiredo, L.P., Grana, D., Bordignon, F.L., Santos, M., Roisenberg, M., and Rodrigues, B.B., 2018, Joint Bayesian inversion based on rock-physics prior modeling for the estimation of spatially correlated reservoir properties: Geophysics, v. 83, no. 5, p. M49–M61.

1049 Dodds, K., Krahenbuhl, R., Reitz, A., Li, Y., and Hovorka, S., 2013, Evaluating time-lapse
1050 borehole gravity for $CO_2$ plume detection at SECARB Cranfield: International Journal of
1051 Greenhouse Gas Control, v. 18, p. 421–429.
1052 Domenico, S.N., 1976, Effect of brine–gas mixture on velocity in an unconsolidated sand
1053 reservoir: Geophysics, v. 41, p. 882–894.
1054 Dupuy, B., Romdhane, A., Eliasson, P., Querendez, E., Yan, H., Torres, V. A., and Ghaderi, A.,
1055 2017, Quantitative seismic characterization of $CO_2$ at the Sleipner storage site, North Sea:
1056 Interpretation, v. 5, no. 4, p. S23–S42.
1057 Dvorkin, J., and Gutierrez, M.A., 2002, Grain sorting, porosity, and elasticity: Petrophysics, v. 43,
1058 no. 3, p. 185–196.
1059 Dvorkin, J., and Nur, A., 1996, Elasticity of high porosity sandstones: Theory for two North Sea
1060 datasets: Geophysics, v. 61, p. 1363–1370.
1061 Dvorkin, J., Nur, A., and Yin, H, 1994, Effective properties of cemented granular material:
1062 Mechanics of Materials, v. 18, p. 351–366.
1063 Eylands, K.E., Kurz, B.A., Hamling, J.A., Heebnik, L.V., Smith, S.A., LaBonte, J.A., Mibeck,
1064 B.A.F., Kleven, P.L., Klapperich, R.J., Braunberger, J.R., and Gorecki, C.D., 2013, Bell
1065 Creek 05-06 OW sidewall core mineralogy assessment: 2013-EERC-04-02 Report.
1066 Fjeldstad, T. and Grana, D., 2018, Joint probabilistic petrophysics-seismic inversion based on
1067 Gaussian mixture and Markov chain prior models: Geophysics, v. 83, no. 1, p. R31–R42.
1068 Furre, A., Eiken, O., Alnes, H., Vevatne, J., and Kiær, F., 2017, 20 years of monitoring $CO_2$
1069 injection at Sleipner: Energy Procedia, v. 114, p. 3916–3926.
1070 Gassmann, F., 1951, Elastic waves through a packing of spheres: Geophysics, v. 16, no. 4, p. 673–
1071 685.

1072 Grana, D., 2018, Joint facies and reservoir properties inversion, Geophysics, v. 83, no. 3, p. M15–
1073 M24.
1074 Grana, D., Fjeldstad, T. and Omre, H., 2017, Bayesian Gaussian mixture linear inversion for
1075 geophysical inverse problems: Mathematical Geosciences, v. 49, p. 493–515.
1076 Greenberg, M.L. and Castagna, J.P., 1992, Shear-wave velocity estimation in porous rocks—
1077 theoretical formulation, preliminary verification and applications: Geophysical Prospecting,
1078 v. 40, p. 195–209.
1079 Gunning, J., and Glinsky, M.E., 2007, Detection of reservoir quality using Bayesian seismic
1080 inversion: Geophysics, v. 72, no. 3, p. R37–R49.
1081 Gunning, J., and Huntbatch, N., 2020, Joint facies/elastic inversion—the importance of
1082 optimisation: 1st EAGE Conference on Seismic Inversion, 26–29 October 2020, Online.
1083 Gunning, J., and Sams, M., 2018, Joint facies and rock properties Bayesian amplitude-versus-offset
1084 inversin using Markov random fields: Geophysical Prospecting, v. 66, p. 904–919.
1085 Hamling, J.A., Gorecki, C.D., Klapperich, R.J., Saini, D., and Steadman, E.N., 2013, Overview of the
1086 Bell Creek combined $CO_2$ storage and $CO_2$ enhanced oil recovery project: Energy Procedia, v.
1087 37, p. 6402–6411.
1088 Han, D., and Batzle, M., 2014, FLAG fluid calculator: University of Houston Fluid/DHI
1089 Consortium.
1090 Han, D., and Sun, M., 2013, Velocity and density of water with dissolved $CH_4$ and $CO_2$: SEG
1091 Annual International Meeting, Expanded Abstracts.
1092 Han, D., Sun, M., and Liu, J., 2012, Velocity and density of $CO_2$–oil miscible mixtures: SEG
1093 Annual International Meeting, Expanded Abstracts.

1094 Honarpour, M., Szpakiewicz, M., Sharma, B., Chang, M.-M., Schatzinger, R., Jackson, S.,
1095 Tomutsa, L., and Maerefat, N., 1989, Integrated reservoir assessment and characterization:
1096 Final report, October 1, 1985 – September 30, 1988.
1097 Jin, L., Bosshart, N.W., Oster, B.S., Hawthorne, S.B., Peterson, K.J., Burton-Kelly, M.E., Feole,
1098 I.K., Jiang, T., Pekot, L.J., Peck, W.D., Ayash, S.C., and Gorecki, C.D., 2016, Bell Creek
1099 test site – simulation report: Plains $CO_2$ Reduction (PCOR) Partnership Phase III draft Task
1100 9 Deliverable D66 (Update 6) executive summary for U.S. Department of Energy National
1101 Energy Technology Laboratory Cooperative Agreement No. DE-FC26-05NT42592, Grand
1102 Forks, North Dakota, Energy & Environmental Research Center, August.
1103 Kemper, M., and Gunning, J., 2014, Joint impedance and facies inversion—seismic inversion
1104 redefined: First Break, v. 32, p. 89–95.
1105 Kemper, M., Paiva, M., and Waters, K., 2017, Facies-based inversion through the asset lifecycle:
1106 15th International Congress of the Brazilian Geophysical Society, p. 1–4.
1107 Kolbjørnsen, O., Buland, A., Hauge, R., Røe, P., Jullum, M., Metcalfe, R.W., and Skjæveland, Ø.,
1108 2016, Bayesian AVO inversion to rock properties using a local neighborhood in a spatial
1109 prior model: The Leading Edge, v. 35, no. 5, p. 431–436.
1110 Landrø, M., 2001, Discrimination between pressure and fluid saturation changes from time-lapse
1111 seismic data: Geophysics, v. 66, no. 3, p.836–844.
1112 Lumley, D., 2010, 4D seismic monitoring of $CO_2$ sequestration: The Leading Edge, v. 29, no. 2,
1113 p. 150–155.
1114 MacBeth, C., 2004, A classification for the pressure-sensitivity properties of a sandstone rock
1115 frame: Geophysics, v. 69, no. 2, p. 497–510.

1116 Macquet, M., Lawton, D.C., Saeedfar, A., and Osadetz, K.G., 2019, A feasibility study for
1117 detection thresholds of $CO_2$ at shallow depths at the CaMI Field Research Station, Newell
1118 County, Alberta, Canada: Petroleum Geoscience, v. 25, no. 4, p. 509–518.
1119 Marion, D., Nur, A., Yin, H., and Han, D., 1992, Compressional velocity and porosity in sand-clay
1120 mixtures: Geophysics, v. 57, no. 4, p. 554–563.
1121 Mavko, G., and Mukerji, T., 1995, Pore space compressibility and Gassmann's relation:
1122 Geophysics, v. 56, p. 1940-1949.
1123 Mavko, G., Mukerji, T., and Dvorkin, J., 2009, The rock physics handbook—tools for analyzing
1124 seismic properties: Cambridge University Press.
1125 Molnar, P.S., and Porter, M.L., 1990, Geologic reservoir study of the Bell Creek Field, Carter and
1126 Powder River Counties, Montana: Exxon Company, Midland, Texas.
1127 Mur, A., Barajas-Olalde, C., Adams, D.C., Jin, L., He, J., Hamling, J.A., and Gorecki, C.D., 2020,
1128 Integrated simulation to seismic and seismic reservoir characterization in a $CO_2$ EOR
1129 monitoring application: The Leading Edge, v. 38, p. 668–678.
1130 O'Brien, J., Moran, J., Wilbourn, G., Morris, S., Andersen, J., and Quezada, O., 2010, Monitoring
1131 a $CO_2$ flood with fine time steps—Salt Creek 4D: Leading Edge, v. 29, no. 8, p. 912–919.
1132 Park, J., Fawad, M., Viken, I., Aker, E., and Bjørnarå, T.I., 2013, CSEM sensitivity study for
1133 Sleipner $CO_2$-injection monitoring: Energy Procedia, v. 37, p. 4199–4206.
1134 Pasternack, E., 2009, Bell Creek petrophysics: Outsource Petrophysics Inc.
1135 Pevzner, R., Isaenkov, R., Yavuz, S., Yurikov, A., Tertyshnikov, K., Shashkin, P., Gurevich, B.,
1136 Correa, J., Glubokovskikh, S., Wood, T., Freifeld, B., and Barraclough, P., 2021, Seismic
1137 monitoring of a small $CO_2$ injection using a multi-well DAS array—operations and initial

results of Stage 3 of the CO2CRC Otway project: International Journal of Greenhouse Gas Control, v. 110, p. 1–14.

Prasad, M., Glubokovskikh, S., Daley, T, Oduwole, S., and Harbert, W., 2021, CO messes with rock physics: The Leading Edge, v. 40, no. 6, p. 424–432.

Rimstad, K., Avseth, P., and Omre, H., 2012, Hierarchical Bayesian lithology/fluid prediction—a North Sea case study: Geophysics, v. 77, no. 2, p. B69–B85.

Roach, L.A.N., White, D.J., Roberts, B., and Angus, D., 2017, Initial 4D seismic results after $CO_2$ injection start-up at the Aquistore storage site: Geophysics, v. 82, no. 3, p. B95–B107.

Salako, O., Jin, L., Barajas-Olalde, C., Hamling, J.A., and Gorecki, C.D., 2018, Implementing adaptive scaling and dynamic well tie for quantitative 4-D seismic evaluation of a reservoir subjected to $CO_2$ enhanced oil recovery and associated storage: International Journal of Greenhouse Gas Control, v. 78, p. 306–326.

Salako, O., Jin, L., Burnison, S.A., Hamling, J.A., Gorecki, C.D., Reed, S. Richards, T., 2017, The value of 4-D seismic monitoring at Bell Creek—a mature oil field undergoing $CO_2$ enhanced oil recovery: 79th European Association of Geoscientists and Engineers Conference 539 & Exhibition.

Sams, M., Weslake, S., Thorp, J., and Zadeh, E., 2016, Willem 3D—eprocessed, inverted, revitalized: The Leading Edge, v. 35, no. 1, p. 22–26.

Sams, M., and Carter, D., 2017, Stuck between a rock and a reflection—a tutorial on low-frequency models for seismic inversion: Interpretation, v. 5, no. 2, p. B17–B27.

Saini, D., Braunberger, J.R., Pu, H., Bailey, T.P., Ge, J., Crotty, C.M., Liu, G., Hamling, J.A., Gorecki, C.D., Steadman, E.N., and Harju, J.A., 2012, Bell Creek test site – simulation report: Plains $CO_2$ Reduction (PCOR) Partnership Phase III Task 9 Deliverable D66

Update 1 for U.S. Department of Energy National Energy Tehcnology Laboratory Cooperative Agreement No. DE-FC26-05NT42592, August.

Schmidt-Hattenberger, C., Bergmann, P., Labitzke, T., Wagner,F., and Rippe, D., 2016, Permanent crosshole electrical resistivity tomography (ERT) as an established method for the long-term $CO_2$ monitoring at the Ketzin pilot site: International Journal of Greenhouse Gas Control, v. 52, p. 432–448.

Sen, M.K., and Stoffa, P.L., 2013, Global optimization methods in geophysical inversion: Cambridge University Press.

Sharaf, E.F., and Sheikha, H., 2021, Reservoir characterization and production history matching of Lower Cretaceous, Muddy Formation in Ranch Creek area, Bell Creek oil field, Southeastern Montana, USA: Marine and Petroleum Geology, v. 127, p. 104996.

Spakiewicz, M., Shatzinger, R., Honarpour, M., Tham, M., and Tillman, R., 1988, Geological and engineering evaluation of barrier island and valley-fill lithotypes in Muddy Formation, Bell Creek Field, Montana: Rocky Mountain Association of Geologists Guidebook, p. 159–182.

Sutherland, R.B., 2011, Bell Creek petrophysical analysis notes: Denbury internal report.

Tarantola, A., 2005, Inverse Problem Theory: Elsevier Science.

Trautz, R., Daley, T., Miller, D., Robertson, M., Koperna, G., and Riestenberg, D., 2020, Geophysical monitoring using active seismic techniques at the Citronelle Alabama $CO_2$ storage demonstration site: International Journal of Greenhouse Gas Control, v. 99, p. 103084,

Tucker, O., Gray, L., Maas, W., and O'Brien, S., 2016, Quest commercial scale CCS – the first year: International Petroleum Technology Conference, Bangkok.

1183 Ulvmoen, M., and Omre, H., 2010, Improved resolution in Bayesian lithology/fluid inversion from
1184 prestack seismic data and well observations—Part 1 — methodology: Geophysics, v. 75,
1185 no. 2, p. R21–R35.
1186 Wan L., Han M., Al Janobi H.A., and Zhdanov M.S., 2018, Feasibility study of gravity
1187 gradiometry monitoring of $CO_2$ sequestration in deep reservoirs using surface and borehole
1188 data: SEG International Exposition and 88th Annual Meeting, p. 1450–1454.
1189 Waters, K., and Kemper, M., 2018, Multi-scenario multi-realisation seismic inversion for
1190 probabilistic seismic reservoir characterisation: 80th EAGE Conference & Exhibition 2018,
1191 11–14 June 2018, Copenhagen, Denmark.
1192 Waters, K., Kemper, M., and Gunning, J., 2019, Facies based Bayesian pre-stack seismic inversion
1193 in the depth domain: 81st EAGE Conference & Exhibition 2019, 3–6 June 2019, London,
1194 United Kingdom.
1195 Waters, K., Somoza, A., Byerley, G., and Rose, P., 2016, Detecting by-passed pay from 3D seismic
1196 data using a facies based Bayesian seismic inversion, Forties Field, UKCS: SEG
1197 International Exposition and 86th Annual Meeting, Expanded Abstracts, p. 2871–2875.
1198 White, D., 2011, Geophysical monitoring of the Weyburn $CO_2$ flood: results during 10 years of
1199 injection: Energy Procedia, v. 4 , p. 3628–3635.
1200 White, D., 2009, Monitoring $CO_2$ storage during EOR at the Weyburn–Midale Field: The Leading
1201 Edge, v. 28, p. 838–842.
1202 White, D., Daley, T.M., Paulsson, B., and Harbert, W., 2021, Borehole seismic methods for
1203 geologic $CO_2$ storage monitoring: The Leading Edge, v. 40, p. 434–441.
1204 White, R.E., 1997, The accuracy of well ties—practical procedures and examples: SEG Annual
1205 International Meeting, Expanded Abstracts, v. 2, p. 2126.

Wood, A.B., 1941, A textbook of sound: MacMillan.

Zhao, X., Ma, R., Zhang, F., Zhong, Z., Wang, B., Wang, Y., Li, Y., and Weng, L., 2017, The latest monitoring progress for Shenhua $CO_2$ storage project in China: International Journal of Greenhouse Gas Control, v. 60, p. 199–206.